(NASA-CR-144165) SSME TURBOPUMP TECHNOLOGY IMPROVEMENTS VIA TRANSIENT ROTORDYNAMIC ANALYSIS Final Report, 1 Nov. 1974 - 31 Jan. 1976 (Louisville Univ.) 122 p HC $5.50 CSCL 22B G3/20

N76-16175

Unclas 13578

SPEED SCIENTIFIC SCHOOL

THE SCHOOL OF ENGINEERING AND APPLIED SCIENCE

OF

The University of Louisville
Louisville, Kentucky
40208

1798

FINAL REPORT

NASA CONTRACT NAS8-31233

SSME TURBOPUMP TECHNOLOGY IMPROVEMENTS VIA TRANSIENT ROTORDYNAMIC ANALYSIS

December 1975

FINAL REPORT

NASA CONTRACT NAS8-31233

SSME TURBOPUMP TECHNOLOGY IMPROVEMENTS VIA TRANSIENT ROTORDYNAMIC ANALYSIS

submitted to

George C. Marshall Space Flight Center
National Aeronautics and Space Administration

by

The University of Louisville
Louisville, Kentucky 40208

Dr. Dara W. Childs
Associate Professor of
Mechanical Engineering
Principal Investigator

22 December 1975

LIST OF FIGURES

Page

LIST OF TABLES

TABLE OF CONTENTS

CHAPTER I

1.1 ADMINISTRATIVE INFORMATION

This report covers the work accomplished on N.A.S.A. contract number NAS8-31233 during the time period 11/1/74 through 1/31/76 for the George C. Marshall Space Flight Center, Alabama 35812. The principal investigator for this study was Dr. Dara W. Childs, an Associate Professor of Mechanical Engineering at the University of Louisville. Direction for the study has been provided by Mr. Loren Gross and Mr. Woody Pitsenberger, Marshall Space Flight Center.

1.2 RESEARCH OBJECTIVES AND ABSTRACT

The rotordynamic behavior of the SSME (Space Shuttle Main Engine) HPOTP (High Pressure Oxygen Turbopump) and HPFTP (High Pressure Fuel Pump) have been analyzed in this study, with the following objectives:

(a) The identification of potential rotordynamic problem areas which might arise during operation of these units prior to their testing.

(b) The investigation of alternative procedures for correcting potential rotordynamic problems should they occur.

(c) The development of an adequate analytic and physical understanding of the turbopump rotordynamics to improve the probability of a correct diagnosis of rotordynamic problems from test data.

Improved transient rotordynamic models are developed in this study for both turbopumps based on [1]*. The present study is a continuation of prior rotordynamic studies for the SSME turbopumps [2,3], and is concerned primarily with rotordynamic stability. The transient models developed here employ the results of Black [4-7] and Yamada [8] to model the hydrodynamic forces developed by the SSME turbopump seals. Linear stability analysis is performed for the SSME turbopump rotordynamics models, which includes gyroscopic effects, seal forces, speed-dependent bearing characteristics, and internal rotor damping.

The stability results for the HPFTP are disturbing in that the first mode of the rotor is predicted to be unstable due to seal forces alone with zero internal rotor damping. The addition of internal rotor damping on the order of one percent for the first two modes significantly worsens the situation.

---

* Identifies entry in Reference Section

The following two redesigns were considered for the pump and turbine-end bearing carrier structures to control the predicted rotordynamic instability:

(a) Stiffness asymmetry in the bearing carrier structure was examined, and significantly improves the stability characteristics of the rotor. Specifically, a bearing carrier would be redesigned so that its radial stiffness in two axial orthogonal planes are markedly different. The carriers would then be assembled in the turbopumps so that their major and minor stiffness planes coincide, preferably with the major stiffness plane aligned with the hydrodynamic sideload to reduce steady-state rotor deflections. The adequacy of this approach depends on the degree of rotor instability as determined by hardware testing.

(b) A redesign was also considered for the bearing carrier structures to develope squeeze-film damper surfaces. The results of this phase of the study are mixed. The squeeze-film-dampers improve rotor stability, and in some cases are sufficient to contain or eliminate the rotor instability. However, their capacity in this regard is limited, and they can be overloaded. Kirk and Gunter's nonlinear model for squeeze-film dampers [17] was used to model the squeeze-film damper forces.

A combination of the two redesign approaches was also considered, again with mixed results. The adequacy of a combined approach depends on the degree of rotor instability, and the net improvement from a combination of the two approaches appears to be less than the sum of their improvements taken separately. It is clearly possible to overload a combined stiffness asymmetry/squeeze-film damper design.

Stability results for the HPOTP rotor indicates that it is more stable than the HPFTP rotor, but is also potentially subject to subsynchronous whirling. Transient simulation models have been developed for the analysis of unstable motion of this rotor if test results of the rotor confirm the presence of an unstable subsynchronous whirling mode.

CHAPTER II

ROTORDYNAMIC SEAL ANALYSIS FOR SSME TURBOPUMPS

2.1 THE ANALYSIS OF YAMADA AND BLACK ET AL.

In this study, the work of Black et al [4-7] was used to define the load-deflection properties of axial-flow sealing surfaces in both turbopumps. Black's analysis is in turn based on a seal-flow analysis by Yamada [8], developed for a "plain" seal, resembling a journal bearing in the sense that the seal has neither steps nor annular serrations. A review of the Yamada-Black procedure follows.

The implementation of Black's analysis for load-deflection properties of seals requires the definition of their flow characteristics. Black employs the following relationship from Yamada [8].

$$\Delta P = (1 + \xi + 2\sigma)\rho v^2/2 = C_d \rho v^2/2 \qquad (1)$$

where ξ is a (constant) entry-loss coefficient, ρ is the fluid density, v is the average fluid velocity, and σ is a friction-loss coefficient defined by

$$\sigma = \lambda \ell/\delta \qquad (2)$$

In the above, ℓ is the seal length, δ is the radial clearance, and λ has been defined by Yamada to be the following function of the axial and radial Reynold's numbers (R_a, R_r)

$$\lambda = 0.079\, R_a^{-1/4}\left[1 + \left(\frac{7R_r}{8R_a}\right)^2\right]^{3/8}$$
$$R_a = 2v\delta/\nu, \quad R_r = r\dot{\phi}\delta/\nu \qquad (3)$$

where ν is the fluid's kinematic viscosity, and r is the seal radius.

Black's analysis yields a load-deflection definition of the form

$$-\frac{\lambda}{r\pi\Delta P}\begin{Bmatrix}F_X\\F_Y\end{Bmatrix} = \begin{bmatrix}\tilde{K} & \tilde{k}\\-\tilde{k} & \tilde{K}\end{bmatrix}\begin{Bmatrix}R_X\\R_Y\end{Bmatrix} + \begin{bmatrix}\tilde{C} & \tilde{c}\\-\tilde{c} & \tilde{C}\end{bmatrix}\begin{Bmatrix}\dot{R}_X\\\dot{R}_Y\end{Bmatrix} + \begin{bmatrix}m & 0\\0 & m\end{bmatrix}\begin{Bmatrix}\ddot{R}_X\\\ddot{R}_Y\end{Bmatrix} \tag{4}$$

where $\dot{\phi}$ is the rotor spin velocity, and

$$\tilde{K} = \mu_o - \mu_2\dot{\phi}^2T^2/4,\quad \tilde{k} = \mu_1\dot{\phi}T/2 \tag{5}$$

$$\tilde{C} = \mu_1T;\quad \tilde{c} = \mu_2\dot{\phi}\,T^2,\quad m = \mu_2T^2$$

$$T = \ell/v$$

In addition, the coefficients μ_0, μ_1, μ_2, are a function of the coefficients ξ, σ, and β, where

$$\beta = \left(\frac{7R_r}{8R_a}\right)^2/\left\{1 + \left(\frac{7R_r}{8R}\right)^2\right\} \tag{6}$$

The factor β is included in the analysis to account for the change in the friction factor λ due to a perturbed displacement of the rotor away from a centered position in the seal. Plots of μ_0, μ_1, μ_2 are provided in Fig. 1 for $\xi = 0.5$ (Ref. [5]). These coefficients are comparatively insensitive to reasonable variations in ξ.

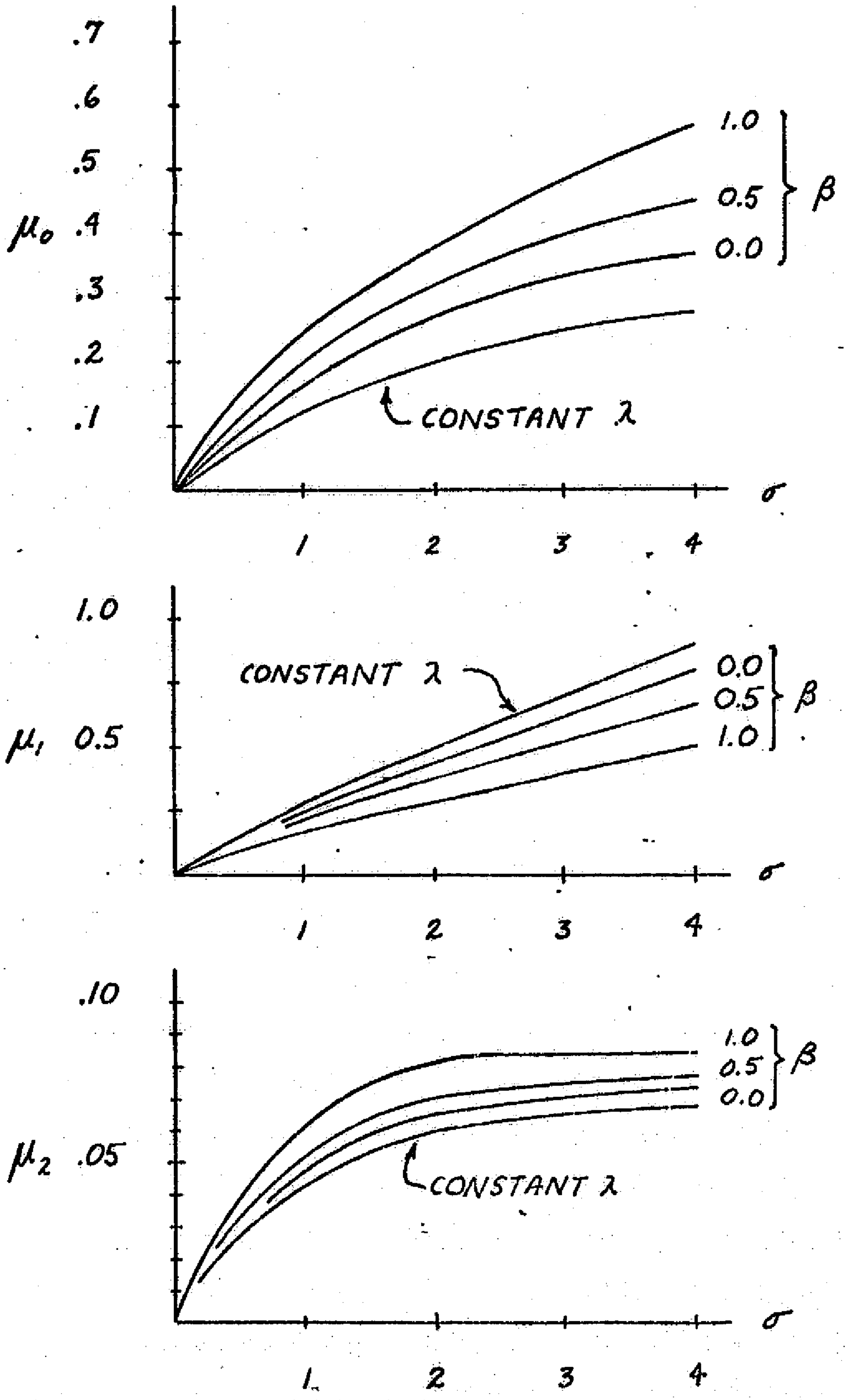

figure 1

Dimensionless flow coefficients μ_0, μ_1, μ_2, versus σ and β for $\xi = 0.5$ taken from reference (5).

Black's analysis accounts for the length of the seal via the following formulae

$$\mu_0(e) = \mu_0/(1 + 0.28\ e^2)$$
$$\mu_1(e) = \mu_1/(1 + 0.23\ e^2) \qquad (7)$$
$$\mu_2(e) = \mu_2/(1 + 0.06\ e^2)$$

where $e = \ell/r$.

2.2 SSME SEAL-FLOW ANALYSIS PROCEDURE

As noted previously, Yamada's flow analysis was developed for "plain" seals, which basically look like journal bearings. The seals in the high pressure SSME turbopumps are not generally of this configuration, since they employ both steps and annular serrations. This section deals with the analysis procedure which was developed to "fit" the results of Yamada's analysis to the SSME seals.

Yamada's analysis can be used to iteratively calculate the leakage flowrate through a seal for a specified differential pressure ΔP and a specified entry loss coefficient ξ. Specifically, one assumes a value for λ, calculates σ from Eq. (2), v from Eq. (1), and then calculates a new value for λ from Eq. (3). This procedure can be repeated until "stable" values for λ and v are achieved. However, this procedure was not initially followed in the present study. Instead, Rocketdyne personnel supplied leakage flowrates, and differential pressure data for each seal at FPL. The calculations which yielded this data were based on Rocketdyne's considerable past experiences with the type of seals used in the turbopumps, and accounted for the reduction in radial clearances due to the centrifugally induced growth of the rotating assembly.

The assumption was made in fitting the Rocketdyne FPL leakage data to the Yamada seal model that the Yamada results were valid for the constant-clearance, constant-radius segments of seals. The data were fitted to the [illegible] model by calculating the (average) velocity at each segment within the seal, and distributing the total ΔP across the seal to each segment on a v^2 basis. Then for each segment within the seal, Eq. (3) is used to calculate σ, and the entrance loss coefficient ξ is calculated from Eq. (1) to satisfy ΔP and v^2 (Rocketdyne data) and σ (Yamada seal model).

The clearances of the seals at FPL speeds used in this study coincided with estimates supplied by Rocketdyne. Where estimates were not provided, the clearances were simply adjusted to yield "reasonable" entry loss coefficients. This adjustment is fairly simple, since for a specified flowrate, the axial Reynolds number R_a is independent of the clearance δ. Thus, λ (and σ) is also largely independent of δ, and Eq. (1) can be used to calculate a suitable average flow velocity v, and δ is selected to yield the prescribed flow rate.

The above procedures yield entrance loss coefficients and friction factors for each segment of each seal at FPL. The following procedure was followed in extrapolating this data across the major portion of the operating speed range of the turbopumps. The following relationships were assumed for the differential pressure across a seal and the seals radial clearance

$$\Delta P = d\dot{\phi}^2, \quad \delta = \delta_0 - b\dot{\phi}^2 \tag{8}$$

where δ_0 is the zero-speed clearance. The constants d and b are calculated for each seal from the known FPL conditions; hence, the values of ΔP and δ are readily calculated for any specified running speed. The entrance-loss coefficients which were calculated for FPL speeds were used at all speeds, and the flow-rate for a specified $\dot{\phi}$ was calculated in the iterative fashion outlined above. Specifically, for a given segment within the seal, ΔP and δ were calculated from Eq. (8), an initial value of λ was assumed, and an average velocity calculated from Eq. (1). Eq. (3) is then used to calculate a new λ, and the cycle is repeated until consistent values of λ and v are obtained. The flow-rate is then calculated from v and δ.

The viscosity and density of the fluid within the seal are required for Yamada's seal analysis. The required data for hydrogen and oxygen were taken from References [9] and [10], respectively, for pressure and temperature data supplied by Rocketdyne personnel. Fluid properties in the turbine areas of the turbopumps were taken from calculations by K. Gross of Marshall Space Flight Center.

The assumptions used here in defining the flow properties of seals are generally supported by the work of Isaacson as reported by Fasheh [11]. Isaacson tested a range of seal teeth configuration and reached the following conclusions:

(a) stepped type labyrinth seals are preferred for leakage control,

(b) stepped type seals are comparatively insensitive to changes in clearances and eccentricities, and

(c) rotational effects on leakage are reduced for large ΔP.

A stepped labyrinth seal is designed to achieve flow constriction primarily by changes in the direction of the flow as opposed to fluid friction losses arising due to viscosity. Hence, conclusion (b) would be anticipated for a properly designed seal, and the implication for the seal model of Eq. (1) is that the friction loss term 2σ would be small in comparison to $(1+\xi)$. Further, Isaacson's test results indicate that the over all seal coefficient C_d (for stepped labyrinth seals) decreases as the axial Reynolds number R_a is increased, and tends to approach an asymptotic value for R_a on the order of $.5 \times 10^5$. This characteristic is interpreted here to mean that the entrance loss coefficient ξ is independent of R_a, and the reduction in C_d results from changes in λ (and hence σ) as defined by Eq. (3).

2.3 SEAL ANALYSIS FOR THE SSME HPFTP

The analysis outlined in the preceeding section was carried out for the HPFTP seals illustrated in figure 2.for the following speed set:

$$\begin{aligned}
\dot{\phi}_1 &= 1654 \text{ rad/sec } (15,800 \text{ rpm}) \\
\dot{\phi}_2 &= 2107 \text{ rad/sec } (20,100 \text{ rpm}) \\
\dot{\phi}_3 &= 2560 \text{ rad/sec } (24,500 \text{ rpm}) \\
\dot{\phi}_4 &= 3016 \text{ rad/sec } (28,800 \text{ rpm}) \\
\dot{\phi}_5 &= 3469 \text{ rad/sec } (33,200 \text{ rpm}) \\
\dot{\phi}_6 &= 3920 \text{ rad/sec } (37,470 \text{ rpm}) = \text{FPL}
\end{aligned} \tag{9}$$

The speed range was selected to include the speed at FPL ($\dot{\phi}_6$ = 3920 rad/sec) and the second critical speed. Table 1 contains a representative set of data and results at FPL. The entries in the second column of this table is the number of constant-clearance constant-radius annular segments used in modeling each seal. The entries in the ΔP column were supplied by Rocketdyne, and the radial clearances at FPL are generally based on Rocketdyne estimates. The axial position entries in Table 1 are with respect to the pump end of the turbopump.

The viscosity, specific weight, and flowrate of the fluid within the seals for the speed set of Eq. (9) are given in Tables 2, 3, and 4, respectively. The FPL flowrate in Table 4 was provided by Rocketdyne. The remaining flowrates were calculated by the method outlined in the preceding section. The results for some of these seals are con-

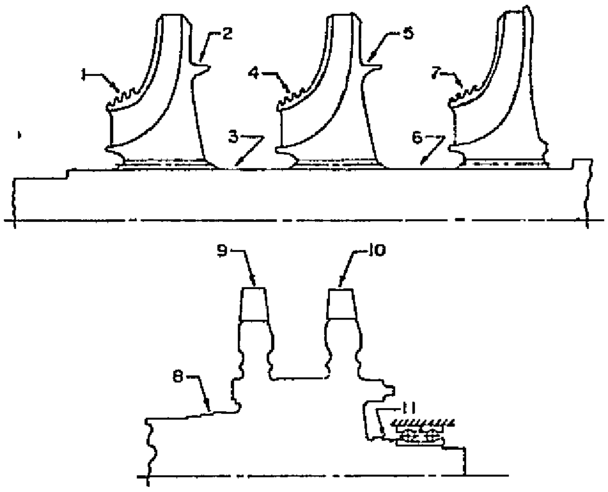

figure 2
HPFTP seal locations

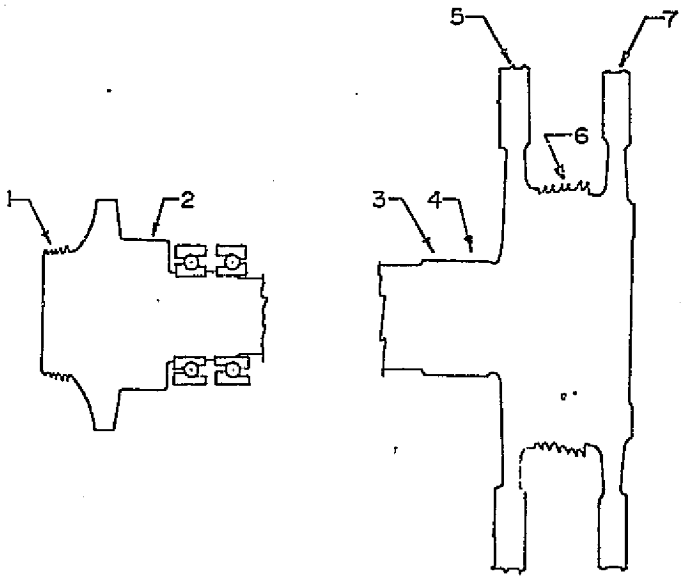

figure 3
HPOTP seal locations

TABLE 1: HPFTP Seal Data and Results at FPL

Seal No.	No. Segments	Axial Position (in.)	ΔP (Psi)	δ (in.)	ξ	σ	$R_r \times 10^{-5}$	$R_a \times 10^{-5}$
1	4	5.25	1325.	.005	0.51	0.025	2.01	2.21
2	3	7.42	980.	.005	0.99	0.029	3.29	2.58
3	3	8.50	1980.	.005	0.38	0.265	1.27	4.28
4	4	10.16	1153.	.005	0.32	0.025	2.67	2.89
5	3	12.37	956.	.005	0.95	0.030	3.10	2.34
6	3	13.33	1990.	.005	0.53	0.315	1.14	3.54
7	4	15.13	1319.	.005	0.43	0.024	2.38	2.64
8	9	20.37	335.	.005	1.48	0.014	1.48	0.908
9	1	22.25	359.	.010	0.39	0.045	0.671	1.26
10	1	24.88	485.	.005	0.67	0.062	0.702	1.25
11	3	25.79	245.	.006	0.28	0.125	1.09	2.42

Table 2: HPFTP Seal Viscosity $(lb_m/ft\ sec) \times 10^5$ at the Selected Operating Speeds of Eq. (9)

Seal No.	FPL	$\dot{\phi}_5$	$\dot{\phi}_4$	$\dot{\phi}_3$	$\dot{\phi}_2$	$\dot{\phi}_1$
1	1.150	1.088	1.029	0.969	0.924	0.887
2	0.827	0.760	0.713	0.657	0.611	0.570
3	0.710	0.644	0.578	0.517	0.448	0.398
4	0.890	0.790	0.682	0.548	0.483	0.356
5	0.930	0.816	0.687	0.548	0.499	0.384
6	0.852	0.740	0.636	0.530	0.426	0.310
7	1.002	0.851	0.720	0.594	0.478	0.352
8	0.698	0.616	0.576	0.410	0.341	0.275
9	1.750	1.570	1.450	1.34	1.23	1.10
10	1.780	1.630	1.500	1.38	1.26	1.11
11	0.550	0.487	0.427	0.376	0.335	0.305

Table 3: HPFTP Seal Specific Weight (lb/ft^3) at the Operating Speeds of Eq. (9)

Seal No.	FPL	$\dot{\phi}_5$	$\dot{\phi}_4$	$\dot{\phi}_3$	$\dot{\phi}_2$	$\dot{\phi}_1$
1	4.74	4.67	4.61	4.54	4.48	4.44
2	4.45	4.34	4.23	4.10	3.98	3.86
3	4.25	4.09	3.90	3.69	3.41	2.87
4	4.90	4.50	4.20	3.79	3.54	2.92
5	4.73	4.51	4.21	3.97	3.61	3.04
6	4.60	4.30	4.05	3.69	3.21	2.40
7	4.90	4.60	4.31	3.90	3.42	2.65
8	4.20	3.86	3.74	2.88	2.22	1.94
9	0.78	0.686	0.550	0.411	0.294	0.138
10	0.99	0.833	0.664	0.493	0.348	0.154
11	3.40	3.01	2.530	2.02	1.45	0.927

Table 4: HPFTP Flow Rate (lb/sec) at the Operating Speeds of Eq. (9)

Seal No.	FPL	$\dot{\phi}_5$	$\dot{\phi}_4$	$\dot{\phi}_3$	$\dot{\phi}_2$	$\dot{\phi}_1$
1	2.383	2.8794	3.0853	3.0346	2.7769	2.3561
2	2.519	4.6292	5.8077	6.1796	5.9050	5.1217
3	1.239	1.2665	1.2187	1.1066	0.9415	0.7164
4	2.404	3.3473	3.7796	3.7230	3.4076	2.6860
5	2.587	4.7021	5.7743	6.0609	5.6055	4.5309
6	1.229	1.2380	1.1833	1.0559	0.8721	0.6254
7	2.473	3.4305	3.9368	3.8827	3.4435	2.6306
8	0.301	0.26096	0.22753	0.17224	0.1261	0.0935
9	3.200	2.8640	2.3712	1.8289	1.3238	0.7326
10	3.200	3.3648	3.1308	2.6173	1.9972	1.1204
11	0.375	0.31198	0.24830	0.18779	0.1302	0.0810

trary to one's normal expectations, since the flowrate increases as speed and ΔP decrease. However, for these seals, the radial clearance is simply increasing faster than ΔP is decreasing, with a resultant increase in flow.

The radii and lengths of seal segments were taken from component drawings. The lengths of the segments within the seal are summarized below:

SEAL	LENGTHS (in.)
1	$\ell_i = .030; \quad i = 1, 2, 3, 4$
2	$\ell_i = .030; \quad i = 1, 2, 3$
3	$\ell_1 = .420, \quad \ell_2 = .470, \quad \ell_3 = .516$
4	$\ell_i = .030; \quad i = 1, 2, 3, 4$
5	$\ell_i = .030; \quad i = 1, 2, 3$
6	$\ell_1 = .420, \quad \ell_2 = .470, \quad \ell_3 = .516$
7	$\ell_i = .030; \quad i = 1, 2, 3, 4$
8	$\ell_i = .100; \quad i = 1, 2, \ldots 9$
9	$\ell_1 = .099$
10	$\ell_1 = .1154$
11	$\ell_1 = .215, \quad \ell_2 = .200, \quad \ell_3 = .135$

The segments in seals 3 and 6 are seen to be significantly longer than the segments of the other seals. The segments of these seals closely resemble seals tested by Black and Cochrane [7] in that each segment is finely grooved with comparatively shallow annular serrations. Black and Cochrane suggest for this type of seal that the total length of the seal (including serrations) be used. The other seals of the turbopump generally differ from seals 3 and 6 in that the axial flow segments are separated by either changes in radius or comparatively deep serrations. Hence, for the remaining seals, only the lengths of the segments themselves (excluding serrations) were included in the analysis.

Returning to Table 1, the last four columns contain average values for ξ, σ, R_a, and R_r at FPL for the segments within seals. The values for ξ can be compared to a range of 0.1 to 0.5 cited by Black. The Reynolds numbers in this chart are considerably greater than those achieved by Black experimentally. The σ values for seals 3 and 6 are approximately an order of magnitude higher than any other seals, because of the comparatively long lengths of the segments within these seals.

Tables 5 through 8 contain the physical stiffness and damping coefficients for the HPFTP seals for the speed set of Eq. (9). From Eq. (4) these coefficients are defined by

$$\begin{aligned} K &= \tilde{K}(\pi r \Delta P/\lambda), \quad & k &= \tilde{k}(\pi r \Delta P/\lambda) \\ C &= \tilde{C}(\pi r \Delta P/\lambda), \quad & c &= \tilde{c}(\pi r \Delta P/\lambda) \end{aligned} \tag{10}$$

In calculating these coefficients, the seal segments were assumed to be in parallel, i.e., stiffness and damping coefficients were calculated for individual segments of the seal, and then summed to obtain effective coefficients for the seal. An inspection of the results of Tables 5 through 8 demonstrates that the diagonal coefficients are approximately an order of magnitude greater than the off diagonal

Table 5: HPFTP Seal Diagonal Stiffness Coefficient
K(lb/in) at the Operating Speeds of Eq. (9)

Seal No.	FPL	$\dot{\phi}_5$	$\dot{\phi}_4$	$\dot{\phi}_3$	$\dot{\phi}_2$	$\dot{\phi}_1$
1	1832.	731.	352.	185.	101.	54.5
2	1417.	219.	72.4	31.0	14.9	7.42
3	1.223×10^5	7.658×10^4	4.840×10^4	3.035×10^4	1.851×10^4	1.053×10^4
4	1698.	454.	179.	81.5	41.1	20.0
5	1460.	223.	71.4	29.4	14.1	6.61
6	1.193×10^5	7.402×10^4	4.634×10^4	2.872×10^4	1.734×10^4	9825.
7	1826.	483.	189.	86.8	42.8	20.9
8	26.16	19.3	14.2	9.20	5.95	3.57
9	2218.	1501.	1025.	692.	454.	290.
10	4621.	2173.	1153.	652.	377.	221.
11	2183.	1719,	1313.	963.	674.	438.

Table 6: HPFTP Off-Diagonal Seal Stiffness Coefficient
k(lb/in) at the Operating Speeds of Eq. (9)

Seal No.	FPL	$\dot{\phi}_5$	$\dot{\phi}_4$	$\dot{\phi}_3$	$\dot{\phi}_2$	$\dot{\phi}_1$
1	275.4	159.	97.6	60.1	36.3	20.5
2	168.2	64.1	33.0	18.5	10.5	5.67
3	1.870×10^4	1.343×10^4	9336.	6206.	3866.	2111.
4	315.4	150.	82.6	46.6	26.6	13.5
5	175.6	66.3	33.4	18.4	10.1	5.11
6	1.747×10^4	1.230×10^4	8480.	5534.	3346.	1720.
7	300.9	144.	79.6	44.9	24.9	12.2
8	5.492	4.04	2.95	1.84	1.08	0.615
9	261.8	180.	115.	68.5	37.6	15.3
10	409.1	237.	136.	74.9	38.8	14.8
11	859.7	631.	434.	276.	115.	73.9

ORIGINAL PAGE IS
OF POOR QUALITY

Table 7: HPFTP Diagonal Seal Damping Coefficient C(lb/in/sec) at the Operating Speeds of Eq. (9)

Seal No.	FPL	$\dot{\phi}_5$	$\dot{\phi}_4$	$\dot{\phi}_3$	$\dot{\phi}_2$	$\dot{\phi}_1$
1	0.1405	0.919	.0647	.0470	.0344	.0248
2	0.0858	.0370	.0219	0.0144	0.00995	0.00686
3	9.543	7.74	6.14	4.85	3.67	2.55
4	0.1609	0.0864	0.0547	0.0364	0.0253	0.0163
5	0.0896	0.0382	0.0222	0.0144	0.00961	0.00618
6	8.915	7.09	5.62	4.32	3.18	2.08
7	0.1535	0.0816	0.0528	0.0351	0.0236	0.0148
8	0.0028	0.00233	0.00196	0.00144	0.00102	0.744×10^{-3}
9	0.1336	0.104	0.0765	0.0535	0.0357	0.0185
10	0.2087	0.137	0.0904	0.0585	0.0369	0.0179
11	0.4386	0.364	0.288	0.216	0.147	0.0894

Table 8: HPFTP Off-Diagonal Seal Damping Coefficient c(lb/in/sec) at Selected Operating Speeds

Seal No.	FPL	$\dot{\phi}_5$	$\dot{\phi}_4$	$\dot{\phi}_3$	$\dot{\phi}_2$	$\dot{\phi}_1$
1	$0.820x10^{-4}$	$0.389x10^{-4}$	$0.724x10^{-4}$	$0.142x10^{-4}$	$0.962x10^{-4}$	$0.665x10^{-4}$
2	$0.2862x10^{-3}$	$0.109x10^{-3}$	$0.618x10^{-4}$	$0.396x10^{-4}$	$0.267x10^{-4}$	$0.181x10^{-4}$
3	0.4876	0.326	0.223	0.151	0.105	0.0633
4	$-0.1405x10^{-3}$	$-0.907x10^{-4}$	$-0.597x10^{-4}$	$-0.390x10^{-4}$	$-0.266x10^{-4}$	$-0.158x10^{-4}$
5	$0.2965x10^{-3}$	$0.109x10^{-3}$	$0.593x10^{-4}$	$0.369x10^{-4}$	$0.223x10^{-4}$	$0.137x10^{-4}$
6	0.6232	0.417	0.289	0.195	0.126	0.0688
7	$0.3364x10^{-5}$	$-0.163x10^{-4}$	$-0.139x10^{-4}$	$-0.101x10^{-4}$	$-0.679x10^{-5}$	$-0.389x10^{-5}$
8	$0.1404x10^{-4}$	$0.122x10^{-4}$	$0.922x10^{-5}$	$0.591x10^{-5}$	$0.370x10^{-5}$	$0.251x10^{-5}$
9	$0.1014x10^{-4}$	$0.565x10^{-5}$	$0.999x10^{-6}$	$0.117x10^{-6}$	$0.390x10^{-6}$	$0.800x10^{-6}$
10	$0.7076x10^{-3}$	$0.368x10^{-3}$	$0.799x10^{-3}$	$0.106x10^{-3}$	$0.547x10^{-4}$	$0.178x10^{-4}$
11	$0.9461x10^{-3}$	$0.851x10^{-3}$	$0.757x10^{-3}$	$0.673x10^{-3}$	$0.564x10^{-3}$	$0.417x10^{-3}$

Table 9: HPOTP Seal Data and Results at FPL

Seal No.	No. Segments	Axial Position (in)	ΔP (Psi)	ζ	ξ	σ	$R_r \times 10^{-5}$	$R_a \times 10^{-5}$
1	5	0.58	2099.	.006	0.720	0.137	0.725	0.605
2	3	2.64	6581.	.005	0.78	0.185	0.128	1.27
3	1	19.71	90.	.0025	0.88	0.963	0.0026	0.0456
4	1	20.48	1865.	.0025	1.31	0.591	0.0432	0.859
5	2	21.44	156.	.005	1.13	0.055	0.406	0.323
6	3	22.47	581.	.0125	0.654	0.046	1.01	2.25
7	2	23.64	153.	.005	1.73	0.063	0.517	0.317

coefficients, i.e., $K > k$; $C > c$. Further, the coefficients for seals 3 and 6 are an approximate order of magnitude greater than the coefficients for the other seals. This result is accounted for by the comparatively large values of σ for these seals. The negative values for the cross-coupling damping terms c in Table 8 arise because (contrary to the results of figure 1 from Ref. [5]), for sufficiently small values of σ, μ_2 is negative. However, the magnitude of these coefficients are so small that they have a negligible effect on turbopump rotordynamics irrespective of their sign.

The seal inertia coefficients m of Eq. (4) were not used in the analyses of this investigation. Preliminary calculations indicated that these coefficients were negligibly small for the HPFTP.

2.4 SEAL ANALYSIS FOR THE SSME HPOTP

The analysis outlined in Section 2.2 and applied in the preceding section to the HPFTP was carried out for the HPOTP seals illustrated in figure 3 for the following speed set:

$$\begin{aligned}
\dot{\phi}_1 &= 1345 \text{ rad/sec} = (12{,}860 \text{ rpm}) \\
\dot{\phi}_2 &= 1728 \text{ rad/sec} = (16{,}400 \text{ rpm}) \\
\dot{\phi}_3 &= 2112 \text{ rad/sec} = (20{,}200 \text{ rpm}) \\
\dot{\phi}_4 &= 2496 \text{ rad/sec} = (23{,}900 \text{ rpm}) \\
\dot{\phi}_5 &= 2879 \text{ rad/sec} = (27{,}500 \text{ rpm}) \\
\dot{\phi}_6 &= 3263 \text{ rad/sec} = (31{,}200 \text{ rpm}) = \text{FPL}
\end{aligned} \qquad (11)$$

The speed was selected to include the FPL speed ($\dot{\phi}_6 = 3263$ rad/sec) and the first critical speed. The axial positions of the seals with respect to the pump end, and the number of segments used in modeling each seal are given in Table 9. The lengths of the segments within the seals are summarized below:

SEAL	LENGTHS (in.)
1	$\ell_i = .124; \quad i = 1, \ldots 5$
2	$\ell_1 = .183, \quad \ell_2 = .229, \quad \ell_3 = .229$
3	$\ell_1 = .250$
4	$\ell_1 = .320$
5	$\ell_1 = .035, \quad \ell_2 = .035$
6	$\ell_i = .150; \quad i = 1, 2, 3$
7	$\ell_1 = .035, \quad \ell_2 = .035$

The viscosity and specific weight of fluid within the seals are given in Tables 10 and 11. The fluid within seals 1 and 2 is lox, within seals 3 and 4 is hydrogen, and within seals 5 through 7 is a hot gas mixture of the combustion products.

Seal flowrates at the speed set of Eq. (11) are provided in Table 12. The flowrates at FPL in this chart are Rocketdyne estimates. The remaining flowrates were calculated by the analysis procedure of section 2.2 based on the FPL differential pressure and radial clearance data of Table 9.

Table 9 also provides average values for ξ, σ, R_r, and R_a for the seal segments at FPL. This data generally resembles the data of Table 1 for the HPFTP, except for seal 3. This seal has a low flowrate, which yields low Reynold's numbers, and a large λ. The combination of a large λ and a large length yields a large σ. Seal 4 is the principal turbine

Table 10: HPOTP Seal Viscosity (lbm/ft.sec.) x 10^5 at the Operating Speeds of Eq. (11)

Seal No.	FPL	$\dot{\phi}_5$	$\dot{\phi}_4$	$\dot{\phi}_3$	$\dot{\phi}_2$	$\dot{\phi}_1$
1	20.	18.72	16.60	15.50	14.50	13.70
2	17.	16.15	15.18	14.46	13.81	13.35
3	0.661	0.684	0.684	0.684	0.684	0.684
4	0.683	0.695	0.695	0.695	0.690	0.690
5	1.394	1.304	1.245	1.187	1.128	1.039
6	1.09	1.053	1.037	1.022	1.006	0.990
7	1.45	1.341	1.274	1.207	1.141	1.074

Table 11: HPOTP Seal Specific Weight (lb/ft^3) at the Operating Speeds of Eq. (11)

Seal No.	FPL	$\dot{\phi}_5$	$\dot{\phi}_4$	$\dot{\phi}_3$	$\dot{\phi}_2$	$\dot{\phi}_1$
1	75.	74.7	74.5	72.8	72.2	71.7
2	73.	73.3	72.7	72.2	71.7	71.3
3	0.0238	0.0113	0.0078	.0056	0.0033	0.0023
4	0.4006	0.324	0.240	0.176	0.122	0.073
5	0.909	0.710	0.573	0.435	0.298	0.160
6	1.358	0.993	0.770	0.548	0.325	0.102
7	1.218	0.861	0.681	0.500	0.319	0.139

Table 12: HPOTP Seal Flowrate (lb/sec) at the Operating Speeds of Eq. (11)

Seal No.	FPL	$\dot{\phi}_5$	$\dot{\phi}_4$	$\dot{\phi}_3$	$\dot{\phi}_2$	$\dot{\phi}_1$
1	4.5	4.278	3.942	3.466	2.936	2.125
2	9.5	10.28	10.21	9.60	8.492	6.396
3	0.01	.006	.0043	0.0031	0.0019	0.0011
4	0.20	.160	0.120	0.087	0.059	0.031
5	0.65	0.657	0.627	0.534	0.402	0.228
6	1.851	1.360	1.061	0.771	0.492	0.195
7	0.650	0.680	0.640	0.537	0.390	0.199

Table 13: HPOTP Seal Diagonal Stiffness Coefficient K(lb/in) at the Operating Speeds of Eq. (11)

Seal No.	FPL	$\dot{\phi}_5$	$\dot{\phi}_4$	$\dot{\phi}_3$	$\dot{\phi}_2$	$\dot{\phi}_1$
1	1.489×10^4	1.016×10^4	6810.	4514.	2875.	1507.
2	1.418×10^5	9.176×10^4	5.998×10^4	3.893×10^4	2.441×10^4	1.268×10^4
3	5921.	4524.	3334.	2343.	1529.	943.4
4	1.403×10^5	1.089×10^5	8.204×10^4	5.919×10^4	4.008×10^4	2.286×10^4
5	564.0	224.3	110.5	59.05	32.48	15.49
6	1973.	1394.	1049.	769.7	546.6	324.1
7	487.1	210.0	102.7	54.35	29.67	14.29

Table 14: HPOTP Seal Off-Diagonal Stiffness Coefficient k(lb/in) at the Operating Speeds of Eq. (11)

Seal No.	FPL	$\dot{\phi}_5$	$\dot{\phi}_4$	$\dot{\phi}_3$	$\dot{\phi}_2$	$\dot{\phi}_1$
1	4968.	3653.	2620.	1731.	1147.	509.2
2	$2.462\text{x}10^4$	$1.946\text{x}10^4$	$1.454\text{x}10^4$	$1.029\text{x}10^4$	6775.	3187.
3	31.54	15.69	9.321	5.392	2.584	1.058
4	1090.	7391.	461.4	272.8	145.9	52.65
5	30.03	14.41	8.060	4.390	2.195	0.705
6	474.6	264.2	170.5	100.7	50.72	12.49
7	23.88	13.79	7.632	4.085	1.972	6.570

Table 15: HPOTP Seal Diagonal Damping Coefficient C(lb/in/sec) at the Operating Speeds of Eq. (11)

Seal No.	FPL	$\dot{\phi}_5$	$\dot{\phi}_4$	$\dot{\phi}_3$	$\dot{\phi}_2$	$\dot{\phi}_1$
1	3.045	2.538	2.101	1.687	1.328	0.757
2	15.09	13.51	11.66	9.742	7.841	4.739
3	0.0193	0.0109	0.00747	0.00510	0.0030	0.00157
4	0.668	0.513	0.370	0.258	0.168	0.0783
5	0.0184	0.0100	0.00646	0.00415	0.00254	0.00104
6	0.291	0.183	0.137	0.0953	0.0587	0.0186
7	0.0147	0.00957	0.00611	0.00387	0.00228	$0.848\text{x}10^{-3}$

Table 16: HPOTP Seal Off-Diagonal Damping Coefficient c(lb/in/sec) at the Operating Speeds of Eq. (11)

Seal No.	FPL	$\dot{\phi}_5$	$\dot{\phi}_4$	$\dot{\phi}_3$	$\dot{\phi}_2$	$\dot{\phi}_1$
1	0.152	0.120	0.0953	0.0740	0.0574	0.0574
2	0.803	0.519	0.333	0.216	0.140	0.167
3	0.287×10^{-3}	0.118×10^{-3}	0.693×10^{-4}	0.416×10^{-4}	0.196×10^{-4}	0.111×10^{-4}
4	0.0105	0.00739	0.00470	0.00290	0.00164	0.769×10^{-4}
5	0.753×10^{-4}	0.390×10^{-4}	0.218×10^{-4}	0.120×10^{-4}	0.601×10^{-5}	0.251×10^{-5}
6	0.00164	0.00142	0.940×10^{-3}	0.563×10^{-3}	0.275×10^{-3}	0.864×10^{-4}
7	0.111×10^{-3}	0.486×10^{-4}	0.267×10^{-4}	0.142×10^{-4}	0.664×10^{-5}	0.216×10^{-5}

floating-ring seal, and at FPL is choked. Hence, the ΔP cited in Table 9 accounts only for the pressure drop due to an entrance loss and fluid viscosity.

Tables 13 through 16 contain the direct and cross-coupled stiffness (K, k) and damping coefficients (C, c) for the HPOTP seals. An examination of Table 13 indicates that the K values for seals 2 and 4 are significantly larger than for the other seals. This result is explained by longer lengths and larger ΔP's for these seals. For the remaining coefficients (k, C, c), seal 2 is dominant, while the magnitudes of coefficients for seal 4 are much reduced. The reduction in magnitude of these coefficients for seal 4 is explained by the differences in the functions μ_0 and μ_1 and the dependence of the coefficients (k, C, c) on the transit time T defined by

$T = \ell/v = \ell\gamma A/\dot{w}$

γ = specific weight

A = flow area

$\dot{w}$ = weight flow rate

The ratio of $\gamma/\dot{w}$ is larger for the lox of seals 1 and 2 than for the liquid hydrogen of seal 4.

CHAPTER III

LINEAR STABILITY ANALYSIS FOR SSME TURBOPUMPS

3.1 INTRODUCTION

The vibration or precessional motion of a rotor is typcially and ideally at its running speed, i.e., the speed of precession and speed of rotation of a rotor are equal. This mode of operation is customarily described as "synchronous". The amplitudes associated with synchronous motion are directly proportional to the unbalance, and the customary operational problem associated with synchronous motion is that of operation at or near a "critical speed". This latter condition arises when the running speed of a rotor coincides with a rotor natural frequency, and the large amplitudes associated with critical speed operations are associated with a resonance phenomenon.

By contrast, many rotors have experienced large-amplitude motion associated with unstable subsynchronous whirling. This type of motion typically begins at an operating speed above a critical speed. As the running speed is increased, the amplitude of subsynchronous motion increases, frequently leading to hardware failures. The characteristics of this unstable motion are independent of the imbalance, and can arise due to a variety of physical mechanisms. A partial listing of these mechanisms follows:

(a) Hysteretic or internal friction damping due to shrink fits, friction in gear type couplings, or material damping.

(b) Hydrodynamic fluid film bearings and seals.

(c) Aerodynamic cross coupling forces.

(d) Dry friction whirl (rubbing).

An excellent survey of rotor-bearing stability is provided in Ref. [12] by Gunter.

Historically, flexible rotors supported on flexible bearings have been prone to unstable whirling modes. Specifically, rotors which are operated at speeds that are much higher than rotor critical speeds are more likely to experience unstable whirling motion. Both of the high pressure SSME turbopumps have top operating speeds which are considerably above their first critical speeds, and are potentially subject to unstable whirling motion. This is particularly true of the HPFTP, which employs a soft bearing support system. The analysis procedure developed in this study to examine the linear stability characteristics of the SSME turbopumps is discussed in the following section.

3.2 LINEAR STABILITY ANALYSIS PROCEDURE

The analysis procedure developed in this study is probably similar to that outlined by Black [4]. However, a lack of detailed discussion in Black's paper makes a direct comparison difficult.

The linear stability analysis to be developed here will be based on the "conventional" modal Jeffcott model of Appendix A, which accounts for the structural dynamics of the rotor-bearing system. In addition, the analysis will account for the seal-force definitions of the preceding chapter, speed-dependent properties of the ball bearings, and asymmetric bearing support stiffness. The appropriate results from Appendix A are

$$\begin{aligned}(\ddot{q}_X) &= (F_X) - \dot{\phi}[CM](\dot{q}_Y) - [2\zeta\lambda]\{(\dot{q}_X) + \dot{\phi}(q_Y)\} \\ &\quad - [\Lambda](q_X) + \dot{\phi}^2(P_X) + \ddot{\phi}(P_Y) \\ (\ddot{q}_Y) &= (F_Y) + \dot{\phi}[CM](\dot{q}_X) - [2\zeta\lambda]\{(\dot{q}_Y) - \dot{\phi}(q_X)\} \\ &\quad - [\Lambda](q_Y) + \dot{\phi}^2(P_Y) - \ddot{\phi}(P_X)\end{aligned} \tag{12}$$

$$\begin{aligned}(F_X) &= [A_e]^T(f_X) + [A_\beta]^T(M_Y) \\ (F_Y) &= [A_e]^T(f_Y) - [A_\beta]^T(M_Y)\end{aligned} \tag{13}$$

$$\begin{aligned}(R_X) &= [A_e]^T(q_X), \quad (R_Y) = [A_e]^T(q_Y) \\ (\dot{R}_X) &= [A_e]^T(\dot{q}_X), \quad (\dot{R}_Y) = [A_e]^T(\dot{q}_Y)\end{aligned} \tag{14}$$

The formulation of Eq. (11) directly accounts for gyroscopic cross-coupling via the [CM] matrix. The matrix $[2\zeta\lambda]$ is diagonal with the elements $2\zeta_i\lambda_i$, and accounts for internal rotor damping. Since the stability of the rotor (as opposed to its response) is of interest, the modal imbalance vectors of Eq. (12) (P_X), (P_Y) can be dropped. The modal force definition of Eq. (13) will be used to account for seal forces and speed-dependent changes in the bearing characteristics. Since no moments are involved, the vectors (M_Y), (M_X) can be dropped from Eq. (13).

Incorporation of the effects of the seal-force definitions of the preceding chapter into the governing differential Eq. (12) is simplified by defining the rotor's position and velocity at seal location as follows

$$(R_{XS}) = [S](q_X), \quad (R_{YS}) = [S](q_Y)$$
$$(\dot{R}_{XS}) = [S](\dot{q}_X), \quad (\dot{R}_{YS}) = [S](\dot{q}_Y) \tag{15}$$

The reduced eigenvector matrix [S] contains the rows of the $[A_e]$ matrix which corresponds to seal locations, and is an nsxm matrix where ns is the number of seals and m is the number of modes retained for integration.

From Eqs. (4) and (10), the components of the seal force at the ith seal are defined by

$$-f_{XSi} = K_i R_{XSi} + k_i R_{YSi} + C_i \dot{R}_{XSi} + c_i \dot{R}_{YSi}$$
$$-f_{YSi} = -k_i R_{XSi} + K_i R_{YSi} - c_i \dot{R}_{XSi} + C_i \dot{R}_{YSi} \tag{16}$$

and the vector of seal forces can be stated

$$(f_{XS}) = [K](R_{XS}) + [k](R_{YS}) + [C](\dot{R}_{XS}) + [c](\dot{R}_{YS})$$
$$(f_{YS}) = -[k](R_{XS}) + [K](R_{YS}) - [c](\dot{R}_{XS}) + [C](\dot{R}_{YS}) \tag{17}$$

where [K], [k], [C], and [c] are diagonal matrices with elements K, k, C, and c, respectively. The modal force definition in terms of the seal forces is

$$(F_X) = [S]^T(f_{XS}), \quad (F_Y) = [S]^T(f_{YS}) \tag{18}$$

From Eqs. (15) and (17), this result becomes

$$-(F_X) = [SK](q_X) + [Sk](q_Y) + [SC](\dot{q}_X) + [Sc](\dot{q}_Y)$$
$$-(F_Y) = -[Sk](q_X) + [SK](q_Y) - [Sc](\dot{q}_X) + [SC](\dot{q}_Y) \tag{19}$$

where

$$[SK] = [S]^T[K][S], \quad [Sk] = [S]^T[k][S]$$
$$[SC] = [S]^T[C][S], \quad [Sc] = [S]^T[c][S] \tag{20}$$

Substitution of Eq. (19) into Eq. (12) will yield the desired differential equations including the effects of seal coefficients.

A development similar to the above is used to account for speed-dependent changes in the bearing stiffnesses, and (where appropriate) changes in the bearing support structure, and yields a modal force definition of the form

$$-(F_X) = [KX](q_X), \quad -(F_Y) = [KY](q_Y) \tag{21}$$

Substitution of Eqs. (19) and (21) into Eq. (12) yields the following homogeneous modal differential equations

$$\begin{aligned}
&(\ddot{q}_X) + \{[2\zeta\lambda] + [SC]\}(\dot{q}_X) + \{\dot{\phi}[CM] + [Sc]\}(\dot{q}_Y) \\
&+ \{[\Lambda] + [SK] + [KX]\}(q_X) + \{\dot{\phi}[2\zeta\lambda] + [Sk]\}(q_Y) = 0 \\
&(\ddot{q}_Y) + \{[2\zeta\lambda] + [SC]\}(\dot{q}_Y) - \{\dot{\phi}[CM] + [Sc]\}(\dot{q}_X) \\
&+ \{[\Lambda] + [SK] + [KY]\}(q_Y) - \{\dot{\phi}[2\zeta\lambda] + [Sk]\}(q_X) = 0
\end{aligned} \tag{22}$$

These equations have the form

$$(\ddot{q}) + [C](\dot{q}) + [K](q) = 0 \tag{23}$$

where

$$(q)^T = \{(q_X)^T, (q_Y)^T\}$$

The substitution $(\dot{q}) = (v)$ reduces the second order matrix differential Eq. (23) to the following first order differential equation

$$\begin{Bmatrix} \dot{v} \\ \dot{q} \end{Bmatrix} + \begin{bmatrix} [C] & [K] \\ -[U] & 0 \end{bmatrix} \begin{Bmatrix} v \\ q \end{Bmatrix} = 0 \tag{24}$$

The eigenvalues of the coefficient matrix in Eq. (24) define the stability properties of the rotor. If m modes are retained in the analysis, the differential Eq. (24) is of 4m order and has 2m sets of complex conjugate eigenvalues; m of these sets correspond to forward processional motion, and m sets correspond to backward precessional motion. A complex-conjugate eigenvalue of the form $-\sigma_i \pm j\omega_i$ indicates that the rotor is unstable, and that its motion will increase exponentially at the frequency ω_i.

3.3 AN APPROXIMATE LINEAR STABILITY ANALYSIS PROCEDURE

Results from the above procedure have the advantage of accuracy in that the effects of all modes are accounted for; however, the results are difficult to interpret physically. Specifically, they indicate that the rotor is either stable or unstable, but do not directly provide insight into the physical mechanisms that either enhance or degrade stability. To gain a better appreciation for the physical mechanisms, the following approximate stability analysis was employed.

The assumption is made that the stability properties of the ith modal pair q_{Xi}, q_{Yi} are independent of the remaining modal coordinates. Hence, from Eq. (22), the governing differential equations for this modal pair are

$$\begin{aligned}
&\ddot{q}_{Xi} + (2\zeta_i\lambda_i + SC_{ii})\,\dot{q}_{Xi} + (\dot{\phi}CM_{ii} + Sc_{ii})\dot{q}_{Yi} \\
&\quad + (\lambda_i{}^2 + SK_{ii} + KX_{ii})q_{Xi} + (2\zeta_i\lambda_i\dot{\phi} + Sk_{ii})q_{Yi} = 0 \\
&\ddot{q}_{Yi} + (2\zeta_i\lambda_i + SC_{ii})\dot{q}_{Yi} - (\dot{\phi}CM_{ii} + Sc_{ii})\dot{q}_{Xi} \\
&\quad + (\lambda_i{}^2 + SK_{ii} + KY_{ii})q_{Yi} - (2\zeta_i\lambda_i\dot{\phi} + Sk_{ii})q_{Xi} = 0
\end{aligned} \tag{25}$$

The assumption that the modal pair q_{Xi}, q_{Yi} are uncoupled from the remaining modal coordinates has been enforced by retaining only the diagonal elements of the matrices [SK],

[Sk], [SC], [Sc], [BK], and [CM].

The characteristic equation for the differential Eq. (25) has the form

$$s^4 + a_1 s^3 + a_2 s^2 + a_3 s + a_4 = 0 \qquad (26)$$

The Routh-Hurwitz conditions for system stability require that the coefficients of this equation a_i be greater than zero, and that the following two conditions be satisfied

$$\Delta_2 = \begin{vmatrix} a_1 & 1 \\ a_3 & a_2 \end{vmatrix} > 0, \quad \Delta_3 = \begin{vmatrix} a_1 & 1 & 0 \\ a_3 & a_2 & a_1 \\ 0 & a_4 & a_3 \end{vmatrix} > 0 \qquad (27)$$

The coefficients a_i are always positive, and the requirements from condition (27) are

$$\begin{aligned} &(\lambda_i^2 + SK_{ii} + \overline{K}_i) + (2\zeta_i \lambda_i + SC_{ii})^2 \\ &\quad + (\dot{\phi} CM_{ii} + Sc_{ii})(\dot{\phi} CM_{ii} + Sc_{ii} - H_i) > 0 \end{aligned} \qquad (28)$$

$$\begin{aligned} &(\delta K_i)^2 / \{(2\zeta_i \lambda_i + SC_{ii})^2 + (\dot{\phi} CM_{ii} + Sc_{ii})^2\} \\ &\quad + (\lambda_i^2 + \overline{K}_i + SK_{ii}) + H_i(\dot{\phi} CM_{ii} + Sc_{ii} - H_i) > 0 \end{aligned} \qquad (29)$$

where

$$\begin{aligned} &2\overline{K}_i = KX_{ii} + KY_{ii}, \quad 2\delta K_i = KX_{ii} - KY_{ii} \\ &H_i = (2\zeta_i \lambda_i \dot{\phi} + Sk_{ii})/(2\zeta_i \lambda_i + SC_{ii}) \end{aligned} \qquad (30)$$

The stability requirement of (28) and (29) are always satisfied if

$$\dot{\phi} CM_{ii} + Sc_{ii} - H_i > 0 \qquad (31)$$

However, for the SSME turbopumps, this condition is normally violated. This point is better appreciated if one notes from Eq. (20) that the modal seal coefficients Sk_{ii}, SC_{ii}

are proportional, respectively, to the physical seal coefficients k_i, c_i. From Eqs. (4), (5), and (10) the physical seal coefficients k_i, c_i are in turn proportional, respectively, to $\mu_1\dot{\phi}T/2$ and $\mu_1 T$. Hence, the coefficient Sk_{ii} is proportional to $\dot{\phi}$, while SC_{ii} is not, and the definition of H_i provided by (29) implies that H_i is also proportional to $\dot{\phi}$. Condition (31) can then be restated as

$$Sc_{ii} + \dot{\phi}(CM_{ii} - h\ )\ \text{[illegible]}\ H_i = \dot{\phi}h_i \tag{32}$$

For the SSME turbopumps, $h_i > CM_{ii}$ which implies that the favorable gyroscopic stiffening effects for these rotors is less pronounced than the combined detrimental effects of internal rotor damping and the seal cross-coupling stiffness coefficients.

Given that condition (32) is violated as $\dot{\phi}$ is increased, condition (29) will normally be violated prior to condition (28). Hence subsequent considerations will be restricted to condition (29), which can be restated as

$$\begin{aligned}&(\delta K_i)^2/\{(2\zeta_i\lambda_i + SC_{ii})^2 + (\dot{\phi}CM_{ii} + Sc_{ii})^2\}\\ &\quad + (\lambda_i^2 + SK_{ii} + \overline{K}_i) + \dot{\phi}h_i CM_{ii} - \dot{\phi}^2 h_i(h_i - CM_{ii}) > 0\end{aligned} \tag{33}$$

The term $\dot{\phi}h_i Sc_{ii}$ is insignificant in this relationship because (a) the modal seal coefficient Sc_{ii} is comparatively small (i.e., $SK_{ii} > Sk_{ii} > SC_{ii} > Sc_{ii}$), and (b) this term is proportional to $\dot{\phi}$, while the right-hand term is proportional to $\dot{\phi}^2$. The first term in (33) arises due to asymmetry in bearing support stiffness and vanishes for a "typical" symmetrically supported rotor. The term $(\lambda_i^2 + SK_{ii} + \overline{K}_i)$

represents the axisymmetric stiffness of the rotor-bearing-seal system. The larger this term, the larger $\dot{\phi}$ must be to cause an onset of instability, which explains in part why stiffer rotors tend to be more stable than flexible rotors, and why instabilities are normally associated with the first or lowest-natural-frequency mode.

The stability criteria (33) includes the effect of gyroscopic stiffening, which was neglected by Gunter and Trumpler [13] in a previous analysis of the effect of stiffness asymmetry. For large $\dot{\phi}$, condition (33) reduces to

$$(\delta k_i/\dot{\phi} CM_{ii})^2 + (\lambda_i^2 + SK_{ii} + \overline{K}_i) - \dot{\phi}^2 h_i (h_i - CM_{ii}) > 0$$

which indicates that the gyroscopic coupling term CM_{ii} reduces the favorable effect of stiffness asymmetry as running speed $\dot{\phi}$ is increased.

3.4 LINEAR STABILITY ANALYSIS FOR THE HPFTP

The analysis procedures of the preceding section were employed to establish the stability characteristics of the SSME turbopumps. The rotordynamic models used for the turbopumps are discussed in References [1] and [2], with supplementary data and discussion provided in Appendix B.

As noted in the preceding section, the eigenvalues of the coefficient matrix in Eq. (24) define the linear stability characteristics of the rotor model. The speed-dependent terms in this matrix arise from the seal coefficient matrices [SK], [Sk], [SC], [Sc], and the speed-dependent changes in the bearing stiffnesses. Changes in the bearings stiffness as a function of speed were obtained directly from Eq. (B.2), and the seal coefficients of Tables 5 through 8 were least-square curvefitted by cubic polynomials in $\dot{\phi}$ for the speed-set of Eq. (9). Specifically, cubic polynomial coefficients were calculated for the coefficients K_i, k_i, C_i, c_i for each seal. A cubic polynomial did a satisfactory job of fitting the coefficients of most seals, particularly the dominant seals 3 and 6.

A computer program was developed to assemble and evaluate the coefficient matrix of Eq. (24), and to subsequently calculate its eigenvalues. The eigenvalue calculation was performed via a QR algorithm using the I.B.M. Scientific Subroutine Package subroutines HSBG and ATEIG.

The results developed in this section demonstrate the dependence of the HPFTP rotor stability on variations in (a) the bearing support stiffness and (b) internal rotor damping. As noted in Appendix B, the HPFTP bearing support has a "design" radial stiffness of

$$k_{Sp}(\text{pump}) = k_{St}(\text{turbine}) = k_S = 2.17 \times 10^5 \text{ lb/in}, \qquad (34)$$

which yields critical speeds at approximately 9,000, 17,500, and 48,000 rpm. The calculation of these critical speeds includes the speed-dependent properties of the bearings and seals.

Tests of the bearing support structure hardware have yielded the following load-deflection data.

load (lb)	deflection (in)	$\overline{k}_S$ (lb/in)
360	2.6×10^{-3}	1.38×10^5
560	3.75×10^{-3}	1.74×10^5
760	4.5×10^{-3}	2.67×10^5
960	5.0×10^{-3}	4.0×10^5

The "stiffness" $\overline{k}_S$ is defined as the change in load divided by the change in deflection, and is the local slope of the load-deflection curve. Deflections greater than .005 in. would exceed available clearances, and are not of interest. The data indicates a significant nonlinear hardening of the bearing support structure as deflection magnitudes are increased. However, this effect is not pronounced over the expected range of deflection magnitudes, which for stable operations would normally be less than .003 in. From the above data and considerations, the bearing support stiffness

$$k_S = 1.4 \times 10^5 \text{ lb/in} \tag{35}$$

was selected as more representative of the actual hardware, and a reasonable lower-bound choice. The calculated critical speeds for this support stiffness are 8,000, 15,200 and 45,500 rpm.

The above cited radial bearing stiffnesses are all axisymmetric following the conventional practice in turbopump design. However, the stability criterion (33) demonstrates that rotor stability can be enhanced by introducing asymmetry into the bearing support structure. This approach has previously been analyzed by Gunter and Trumpler [13], and was investigated here for the following asymmetric support stiffness selection

$$\begin{aligned} k_{SpX} &= 2.3 \times 10^5 \text{ lb/in} \quad & k_{StX} &= 2.3 \times 10^5 \text{ lb/in} \\ k_{SpY} &= 1.38 \times 10^5 \text{ lb/in} \quad & k_{StY} &= 1.38 \times 10^5 \text{ lb/in} \end{aligned} \tag{36}$$

The calculated critical speeds for this set of bearing stiffnesses are approximately 9,100, 17,300, and 50,000 rpm. The bearing stiffness choice in Eq. (36) was obtained by holding k_{SpY}, k_{StY} constant, and increasing k_{SpX}, k_{StX} until the second critical reached its cited value. An additional increase in k_{SpX}, k_{StX} is not desirable, since it would place the second critical speed too near the operating range.

The analysis of the preceding section demonstrates that internal rotor damping, as defined by the modal damping factors ζ_i, acts to destabilize a rotor as $\dot{\phi}$ is increased. Hence the results of stability analysis are strongly dependent on the choice for ζ_i, and for the HPFTP are dependent on the first two modal damping factors ζ_1, ζ_2. From past test and operational experience, Rocketdyne personnel suggest upper bounds for ζ_1, ζ_2 on the order of .01 to .02; however, (as always) the correct value for these factors are highly uncertain. In this section, the choices for internal damping to be considered are (a) $\zeta_1 = \zeta_2 = 0$, and (b) $\zeta_1 = \zeta_2 = .01$, with $\zeta_3 = \zeta_4 = .02$. The true situation is assumed to be bracketed by these values.

The results of stability analysis for the HPFTP rotor with $\zeta_1 = \zeta_2 = 0$ for the axisymmetric stiffnesses of Eqs. (34) and (35) are presented in figure 4(a), and consist of the roots associated with the first two modes at the running speed set of Eq. (9). The results are presented in root-locus format in figure 4(a). Note that the roots are the negative of the eigenvalues; hence, stable and unstable roots are located in the left and right half planes, respectively. The upper and lower half planes are mirror images; hence, only the upper half plane is illustrated. The data marks on the curves denote the speeds of Eq. (9). The results indicate that the second mode is stable over the operation speed range, but the onset speeds of instability for the first mode at $k_S = 2.17 \times 10^5$ lb/in and $k_S = 1.4 \times 10^5$ lb/in are 19,500 and 16,800 rpm, respectively. The predicted whirl frequencies (the frequency at which the rotor would whirl subsynchronously) are 9,850 rpm ($k_S = 2.17 \times 10^5$ lb/in) and 8,500 rpm ($k_S = 1.4 \times 10^5$ lb/in).

Figure 4(b) illustrates the same results as 4(a) except that $\zeta_1 = \zeta_2 = .01$. In this case the first mode is unstable over the entire speed range of Eq. (9), and the onset speeds of instability for the second mode are 22,900 rpm ($k_S = 2.17 \times 10^5$ lb/in) and 19,200 rpm ($k_S = 1.4 \times 10^5$ lb/in). An extrapolation of the results of figure 4(b) yields predicted onset speeds of instability for the first mode at 12,200 rpm ($k_S = 2.17 \times 10^5$ lb/in) and 11,000 rpm ($k_S = 1.4 \times 10^5$ lb/in).

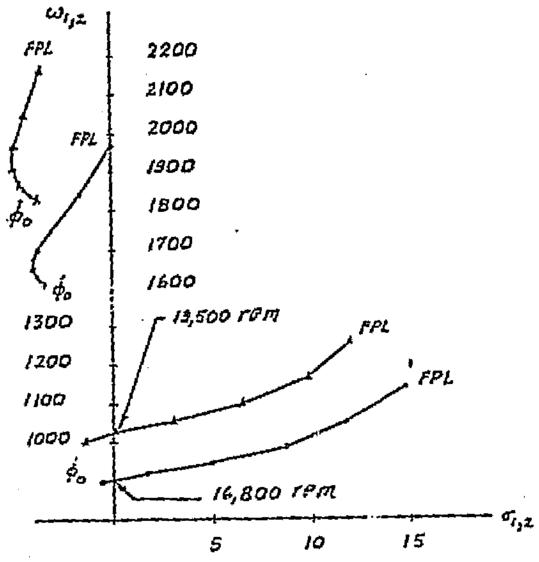

figure 4a

HPFTP stability analysis results for $\zeta_1 = \zeta_2 = 0.0$ and the speed range of Eq. (9) with (a) $k_s = 2.17 \times 10^5$ lb/in —+—+—, and (b) 1.4×10^5 lb/in —o—●—

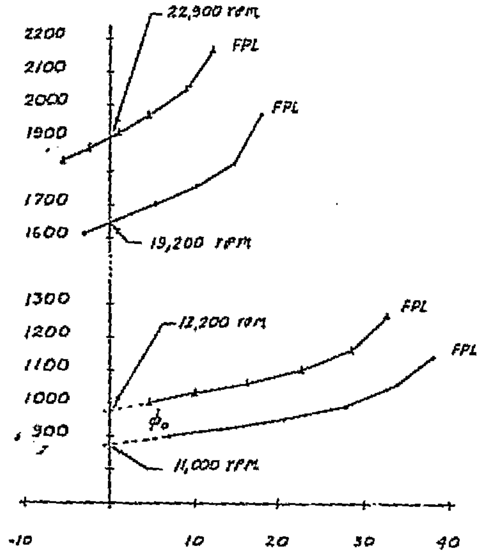

figure 4b

HPFTP stability analysis results for $\zeta_1 = \zeta_2 = 0.01$ and the speed range of Eq. (9) with (a) $k_s = 2.17 \times 10^5$ lb/in —+—+—, and (b) 1.4×10^5 lb/in —o—●—

The results of figures 4(a) and 4(b) were checked by using the approximate stability criterion (33) of Section 3.4 for the first mode. The approximate procedure agreed in all cases with the more exact procedures of Section 3.3.

Note was made in the preceding chapter that the stiffness and damping coefficients for seals 3 and 6 are an order of magnitude larger than the coefficients for the other seals. The above stability analyses were accordingly repeated with the coefficients of all seals except seals 3 and 6 set to zero, with no appreciable change in the results.

The results of figures 4(a) and 4(b) support the following general conclusions:

(a) The HPFTP rotor is predicted to be unstable because of the seals alone (no internal damping).

(b) Rotor stability is extremely sensitive to internal modal damping factors ζ_1, ζ_2.

(c) Feasible increases in the axisymmetric radial stiffness k_S does not have an appreciable influence on rotor stability.

Figure 4(c) illustrates the results of stability analysis for the asymmetric support stiffness set of Eq. (36) with $\zeta_1 = \zeta_2 = 0$, and $\zeta_1 = \zeta_2 = .01$. For $\zeta_1 = \zeta_2 = 0$, the second mode is stable for the speed range of Eq. (9), and the onset speed of instability for the first mode is 32,600 rpm. For $\zeta_1 = \zeta_2 = .01$, the onset speeds of instability for the first and second modes are, respectively, 30,300 rpm and 26,300 rpm. Hence, one has the surprising result that in-

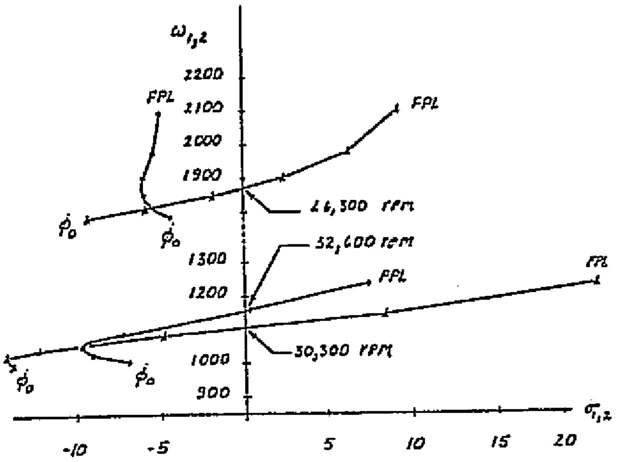

figure 4c

HPFTP stability analysis results for the asymmetric support stiffness choice of Eq. (35) and the speed range of Eq. (9) with (a) $\zeta_1 = \zeta_2 = 0$ —○—○— , and (b) $\bar{\zeta}_1 = \bar{\zeta}_2 = .01$ —△—△—

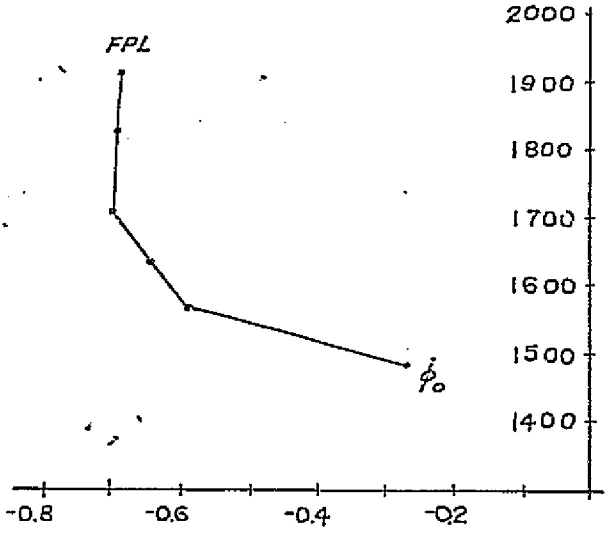

figure 5a

HPOTP stability analysis for $\zeta_1 = 0$ and the speed range of Eq. (11).

ternal damping, while reducing both onset speeds of instability, yields a lower onset speed of instability for the second mode than the first. The explanation for this result is that CM_{11} is an order of magnitude smaller than CM_{22}; hence, from condition (33), the stabilizing effect of asymmetry is more pronounced for the first mode than for the second. A comparison of figure 4(c) with figures 4(a) and 4(b) demonstrates that the introduction of support asymmetry can markedly improve the stability of the HPFTP rotor. However even with the maximum support asymmetry provided by Eq. (36), a rotor instability continues to be predicted.

The nonlinearity of the bearing support structure has the potential of providing some "natural" asymmetry without modification of the bearing carriers. Specifically, a steady-state deflection of the rotor in the X-Z plane due to the hydrodynamic side load causes the support structure to be stiffer in the X-Z plane than in the Y-Z plane. Since the steady state displacement of the turbine bearing is significantly larger than the pump bearing, this nonlinear hardening effect would be felt primarily at the turbine bearing. From these considerations, stability analysis was performed for the HPFTP rotor for the asymmetric support stiffness set

$$k_{SpX} = 1.38 \times 10^5 \text{ lb/in} \qquad k_{StX} = 1.74 \times 10^5 \text{ lb/in}$$

$$k_{SpY} = 1.38 \times 10^5 \text{ lb/in} \qquad k_{StY} = 1.38 \times 10^5 \text{ lb/in}$$

This degree of asymmetry had no appreciable influence on rotor stability.

The results of figures 4(a), (b) are not encouraging, since they generally predict a subsynchronous rotor instability, which has the possibility of serious damage to the turbopump. From past experience, the bleak situation of figure 4(b) seems very unlikely; however, the situation illustrated in figure 4(a) is consistent with past rotor instability experience [15]. Specifically, the predicted onset speeds of instability are approximately twice their associated whirl speeds. From a percentage of critical damping viewpoint, the rotor is never "severely" unstable, e.g., at FPL the percentage of (negative) critical damping in figure 4(a) is on the order of 0.5. The smallness of this value will be immaterial if tests prove the rotor to be unstable; however, it does suggest that small changes in the rotordynamic model could yield a contrary prediction; viz., a stable instead of an unstable rotor.

The principal point of uncertainty in the model which yields a prediction of instability is the stiffness and damping coefficients for the seals. The seal models developed by Black are for a centered position of the shaft relative to the seal. For the HPFTP rotor, the combination of a large side load and soft bearing mounts insures violation of this condition. Black has performed nonlinear calculations (but not tests) which suggest that his linear seal model is reasonable for eccentricity ratios on the order of 0.5; however, the validity of Black's nonlinear "turbulent bulk flow" model can also be questioned. The justifications for using Black's model are (a) it appears to be reasonable and for a centered position is supported by test data, and (b) it is the only model presently available.

In addition to the seal stiffness and damping coefficients and internal rotor damping, rotor stability probably depends on the following additional physical phenomena:

(a) Ball bearing damping. The fact that loaded ball bearings operating at high speeds generate a great deal of heat suggests that ball bearings would be a source of external rotor damping. However, tests of rotors on ball bearings have indicated little or no damping, and a zero-damping assumption is generally followed in rotordynamic analysis

(b) Small radial clearances are provided at the bearings on both turbopumps to allow axial motion of the rotor. These clearances are obviously filled with the working fluid of the pumps, and the annular surfaces associated with these clearances could act like squeeze-film dampers, which would in general improve the stability properties of the rotors. No consideration was made of these clearances in the present study.

(c) Aerodynamic Cross Coupling. Alford [14] has proposed an aerodynamic cross-coupling mechanism as the cause of some rotor instabilities. The physical explanation for this instability is the difference in efficiency of turbine blades in the vicinity of reduced or enlarged clearances due to rotor displacements. However, very little progress has been made since Alford's original paper in apriori calculation of aerodynamic cross-coupling coefficients, and as things now stand this mechanism tends to be invoked to explain rotor instabilities which depend on power levels as well as speed. Presumably, the turbine wheels for the SSME turbopumps could introduce some aerodynamic cross-coupling which would degrade the rotor's stability characteristics; however, no consideration was made in this study of aerodynamic cross-coupling. (Note is made, however, that the analysis procedures of Sections 3.2 and 3.3 can readily account for aerodynamic cross-coupling coefficients.)

If the rotor instability predicted by figures 4a,b is encountered during the SSME test program, the easiest and most direct corrective modification to the turbopump would be the introduction of stiffness asymmetry as illustrated in figure 4c. However, a judgement on the probable success of this approach would have to be based on the measured characteristics of a rotor instability, e.g., onset speed of instability, whirl frequency, rate of divergence etc. In the following chapter, an alternative (or supplementary) approach for the improvement of rotor stability is considered, which involves the attempted development of squeeze-film damper forces at the annular surface between the bearing carriers and the housing of the turbopumps.

The opinion of this investigator is that rotor stability is not likely to be significantly improved by external coulomb damping devices or by feasible modifications of the seals in the HPFTP. Coulomb damping is not generally effective after an instability has been initiated, and seals 3 and 6 presently have configurations which are close to those recommended by Black [4]. Rotor stability could possibly be improved by a program to reduce internal rotor damping by minimizing rubbing. This approach has been followed in dealing with shrink-fitted wheels on steam turbines [15].

3.5 LINEAR STABILITY ANALYSIS RESULTS FOR THE HPOTP

The analysis performed in the preceding section was basically followed here in analyzing the HPOTP rotordynamic stability. The HPOTP rotordynamic model is reviewed in Appendix B. The requisite seal coefficients are provided in Tables 13 through 16, and were curve-fitted via cubic polynomials in $\dot{\phi}$. The definition of speed-dependent changes in the bearing stiffnesses were obtained directly from Eqs. (B.4) and (B.5).

From a rotordynamics viewpoint, the principal difference between the HPOTP and the HPFTP is that the HPOTP does not employ a flexible bearing carrier. With the exception of small radial clearances, which are provided to permit axial motion, the bearings are supported directly by the turbopump housing. By the nature of this simplified design, there is little that can be done to this turbopump to either enhance or degrade its rotordynamic stability.

The first two critical speeds of the HPOTP have been calculated by Rocketdyne to lie at approximately 13,000 and 40,000 rpm. Hence, only the first critical speed lies within the operating range, and only the first forward precessional mode is potentially unstable. The next three modes are comfortably stable for all conditions examined here, and the balance of this discussion will deal exclusively with the first mode.

Figure 5(a) illustrates the results for the first mode of stability analysis with $\zeta_1 = 0.0$ over the speed range of Eq. (11). The results indicate that the rotor is stable over the speeds considered when acted on solely by the seal forces. The predicted first critical speed associated with the results of figure 5(a) is 14,600 rpm. An explanation for the fact that this value is higher than the 13,000 rpm prediction of Rocketdyne is provided by the comparatively large values of the direct stiffness coefficients K_i in Table 13. The stiffness at seal 4 is of particular importance in this regard, since the first-mode eigenvector (Table B.2, Appendix B) has comparatively large deflections associated with the over-hung turbine wheels at this seal location. Hence, the comparatively large direct stiffness at seal 4 location elevates the critical speed.

Figure 5(b) illustrates the results for the first mode of stability analysis with $\zeta_1 = .02$ over the speed range of Eq. (11). The results predict an onset speed of instability at approximately 15,000 rpm, again with the first critical speed at 14,600 rpm. The results of this figure are probably unrealistic, since rotor instabilities are more frequently associated with speeds that are on the order of twice a rotor natural frequency, whereas this predicted instability speed is only slightly greater than its associated critical speed.

The results of figures 5(a) and (b) were checked and confirmed by the stability criterion (33) of Section 3.3.

A comparison of figures 5(a) and (b) emphasizes the dependence of stability on the internal modal damping factor ζ_1. An inspection of Table B.1 of Appendix B demonstrates that the HPOTP first mode is a bending mode as opposed to the first two HPFTP modes which have a rigid-body character. Hence, a comparatively large modal damping factor might be anticipated. However, the basic structural element in the HPOTP rotor is a solid shaft, while the HPFTP rotor is basically a group of wheels held together by a throughbolt. The parts which are concentrically fitted to the outside of the HPOTP rotor outboard of the turbine bearings are not designed to carry a bending load, and the rubbing associated with their interference fit is presumably small. These factors argue for a comparatively small ζ_1, with a consequent improvement in the stability picture.

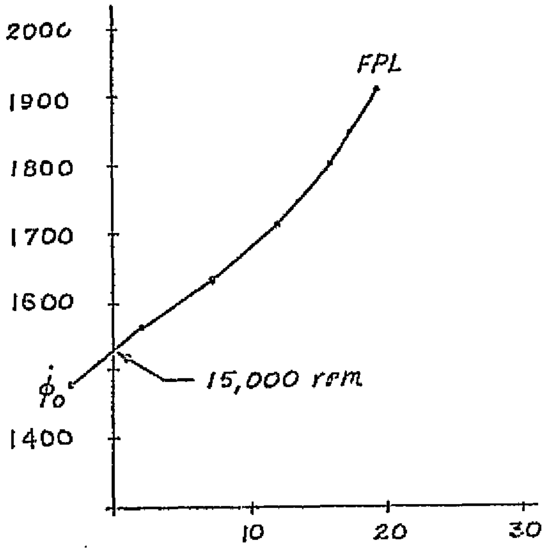

figure 5b

HPOTP stability analysis for $\zeta_1 = 0.02$ and the speed range of Eq. (11).

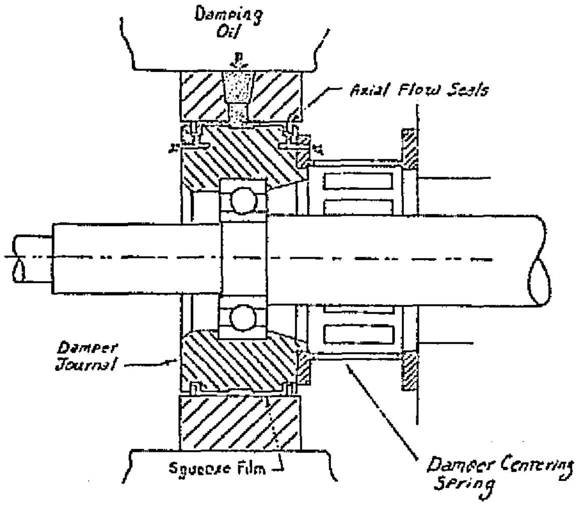

figure 6

Recommended squeeze-film damper design from reference (16).

The linear stability analysis results of this and the preceding section were generated on an I.B.M. 360-165 computer. The computer time requirements for the speed set of Eq. (11) used in analyzing the HPOTP were approximately 8 or 9 seconds, with a comparable time requirement for the HPFTP speed set of Eq. (9).

3.6 SUMMARY

a review of the stability results for the HPFTP and HPOTP supports the following general conclusions.

(a) The HPFTP is probably going to encounter stability problems within its range of operations; however, if an instability is encountered, various procedures can be attempted to improve its stability properties.

(b) The HPOTP is inherently more stable than the HPFTP, and is less likely to experience stability problems over its range of operations. However, if this unit does have an instability problem, there are a limited number of obvious approaches for improving its stability characteristics.

CHAPTER IV

TRANSIENT SIMULATION OF SSME ROTORDYNAMICS

4.1 INTRODUCTION

As noted in the introduction, prior studies by this investigator of SSME rotordynamics [2,3] employed transient simulations to predict amplitudes of rotor motion during critical-speed transitions and at FPL. In these investigations, sufficient external damping was provided to insure stability. The results of the preceding section would suggest that this was an overly optimistic approach, since both turbopumps are predicted to be either very lightly damped or unstable at full-power levels. If the results of Chapter III are in error, and the rotors are in fact stable at full-power levels, the predicted amplitudes of Ref. [2-3] should be reasonable, since the FPL speeds are well removed from critical-speed locations, and are comparatively insensitive to rotor damping. However, if the rotor damping is as low as predicted by the results of Chapter III, the amplitudes of the rotors during critical-speed transitions are going to be significantly larger than predicted in Ref. [2,3]. In particular, the predicted rubbing problem for the HPOTP turbine floating-ring seal during shut-down critical-speed transition will be more severe than previously suggested.

The following results of Chapter III, with regard to rotor stability, established the objectives of transient rotordynamic simulations for the present study.

(a) Very serious stability problems are predicted for the HPFTP, and several alternatives can be considered to improve the situation.

(b) Stability problems are possible for the HPOTP, but less likely than for the HPFTP. Moreover, there are few obvious options presently available to improve the stability characteristics of the HPOTP.

In view of these results, transient rotordynamic investigations of this study were concentrated primarily on the application of squeeze-film dampers to improving the stability characteristics of the HPFTP. A proposed squeeze-film damper design for the HPFTP is discussed in the following section.

4.2 SQUEEZE FILM DAMPER DESIGNS FOR THE HPFTP

Figure 6 is taken from Ref. [16] and illustrates a "typical" squeeze-film damper installation. In this design, the outer race of a ball bearing is attached to a flexibly supported non-rotating cylinder. A squeeze-film damper is contained in the annulus at the outer surface of this cylinder. The fluid is a comparatively viscous oil, which is both pumped into and confined within the annulus. The damping forces developed via a squeeze film damper differ from those developed at a journal bearing because the ball-bearing housing/damper journal is allowed to move radially in response to the rotor's motion, but does not rotate.

The design concept illustrated in figure 6 is clearly not compatible with a liquid oxygen or liquid hydrogen turbopump. Specifically, the problems involved in supplying a separate oil supply in a cryogenic environment would be staggering. However, the design of the bearing carrier structure in the HPFTP is such that its outer surface executes the desired motion of a squeeze film damper, i.e., it precesses in response to the bearing reaction loads, but does not rotate. Hence, a modification of the annulus at the outer surface of the bearing carrier structure as illustrated in figure 7 could yield squeeze film damper surfaces at both bearings in the HPFTP. These designs are certainly not as attractive as the ideal design of figure 6, since the pump-and turbine-end bearings will contain liquid and gaseous hydrogen, as opposed to a comparatively high viscosity oil. Moreover, the hydrogen in these dampers is not pressure-supplied through a central groove, nor is its axial flow constrained by piston rings. These design modifications have the principal advantage of being compatible with the present turbopump design. In the balance of this chapter, the assumption is made that the proposed design modifications of figure 7 have an adequate supply of working fluid.

The modifications of figure 7 use a constant-clearance "conventional" design. An unconventional "partial" squeeze-film damper design was also examined in this stu-

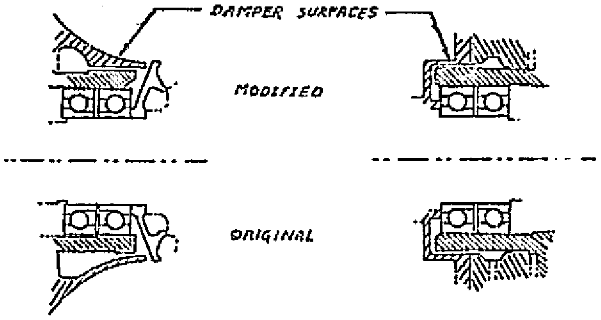

figure 7

Proposed squeeze-film damper design modifications for the HPFTP.

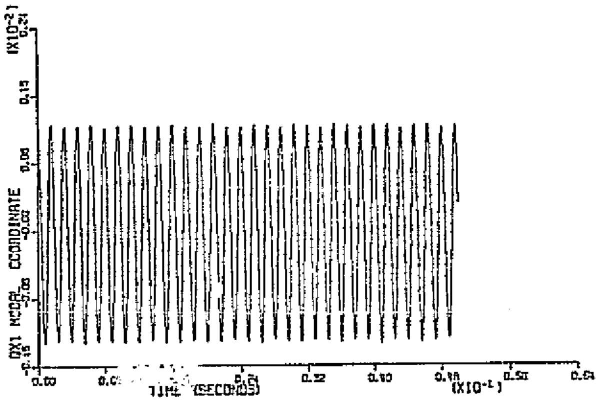

figure 8a

q_{X1} versus time for $k_s = 2.17 \times 10^5$ lb/in; $\zeta_1 = \zeta_2 = 0$.

dy. This design utilizes a much-enlarged radial clearance over half of its circumference. The stability results were indistinguishable for the conventional and partial squeeze-film-damper designs; however, an adequate supply of working fluid would be more easily assured with the partial design.

4.3 HPFTP SQUEEZE FILM DAMPER MODELING

The results of (the excellent) reference [17] by Kirk and Gunter was used here to model the nonlinear load-deflection characteristics of a squeeze-film damper. Kirk and Gunter use the short-bearing approximation to obtain the following definition of the force components acting on a rotor from a squeeze film damper of length ℓ, radial clearance δ, radius r, and fluid viscosity μ

$$\begin{Bmatrix} f_X \\ f_Y \end{Bmatrix} = - \int_0^{2\pi} P(\theta) \begin{Bmatrix} c\theta \\ s\theta \end{Bmatrix} d(\ell r\theta) \qquad (37)$$

In this definition for the force components, the average pressure at angular position , defined by

$$\bar{P}(\theta) = \frac{\mu\ell^2 (\dot{R}_X c\theta + \dot{R}_Y s\theta)}{(\delta - R_X c\theta - R_Y s\theta)^3} \qquad (38)$$

is integrated over the circumference of the squeeze film. In Eq. (38), $c\theta = \cos\theta$, $s\theta = \sin\theta$, and the position and velocity of the squeeze-film damper cylinder are defined respectively by R_X, R_Y and $\dot{R}_X$, $\dot{R}_Y$. The term squeeze-film damper cylinder refers here to the ball-bearing housing/damper journal of figure 6 or the ball-bearing carrier of figure 7. The effect of cavitation is enforced in reference [17] by requiring that the average pressure $\bar{P}(\theta)$ equal or exceed zero. In the present situation the pump-end damper contains gaseous hydrogen at very high pressure, and the turbine-end damper contains liquid hydrogen at approximately 160 psi. (FPL condition). Hence, the assumption is made that neither damper will cavitate. Kirk and Gunter's recommendation of a Newton-Cotes quadrature formula for the evaluation of the integral in Eq. (37) was followed here, with an integration step of $(\pi/30)$ radians.

From a transient simulation viewpoint, the squeeze-film damper reaction definition of Eq. (37) does not basically introduce any new reaction-definition requirements beyond those normally required for a ball-bearing. Specifically, the position and velocity of the damper cylinder is required in Eq. (37), and this is also the normal requirement for a bearing reaction definition. The pump- and turbine-bearing carrier eigenvector entries are, respectively, rows 28 and 29 of Table B.1, Appendix B. As noted in Appendix A, the correct definition of the position of the bearing carrier structures required the use of a residual correction procedure in this study.

The squeeze-film damper reaction definitions of Eq. (37) can be used to obtain direct and cross-coupled stiffness and damping coefficients similar to those of Eq. (4)

for seals. Alternatively, for the purposes of design, "equivalent" direct stiffness and damping coefficients can be calculated as a function of eccentricity ratio ε. The physical and dimensionless stiffness (K_d, $\bar{K}_d$) and damping (R_d, $\bar{R}_d$) coefficients are defined in terms of the eccentricity ratio ε by

$$\begin{aligned} \bar{K}_d &= K_d\delta^3/\mu\dot{\phi}\gamma\ell^3 = 2\varepsilon/(1-\varepsilon^2)^2 \\ \bar{R}_d &= R_d\delta^3/\mu\gamma\ell^3 = \pi/2(1-\varepsilon^2)^{3/2} \end{aligned} \qquad (39)$$

The dimensionless coefficients are obviously nonlinear functions of the eccentricity ratio, which approach an unbounded limit as the eccentricity ratio ε approaches unity.

The unsuitability of hydrogen as a squeeze-film damper fluid can be appreciated by calculating these coefficients for an eccentricity ratio of $\varepsilon = 0.4$, which yields from Eq. (39), $\bar{K}_d = 1.13$; $\bar{R}_d = 2.04$. The remaining data for the HPFTP at FPL are:

$$\begin{aligned} &\dot{\phi} = 3930 \text{ rad/sec},\ r = 1.843 \text{ in}, \\ &\mu(\text{pump end}) = 2.96 \times 10^{-7} \text{lbf sec/ft}^2 = 2.06 \times 10^{-9} \text{lbf sec/in}^2 \\ &\mu(\text{turbine end}) = 2.18 \times 10^{-7} \text{lbf sec/ft}^2 = 1.52 \times 10^{-9} \text{lbf sec/in}^2 \qquad (40) \\ &\ell(\text{pump end}) = \ell(\text{turbine end}) = 1 \text{ in} \end{aligned}$$

From these data, the following physical stiffness and damping coefficients can be calculated

δ (in)	R_d (lb sec/in)	K_d (lb/in)
.001	4.21	16,600.
.002	.526	2,070.
.003	.150	615.

These values are small in comparison to the seal stiffness and damping coefficients of Tables 5 and 7, but from Eq. (39), they increase sharply as the eccentricity ratio increases.

4.4 TRANSIENT SIMULATION OF HPFTP MOTION WITH SQUEEZE-FILM DAMPERS AND AXISYMMETRIC STIFFNESS SUPPORTS

The results of Chapter III demonstrate that the HPFTP rotor becomes progressively less stable as the running speed $\dot{\phi}$ is increased; hence, all transient simulations for the purposes of examining rotor stability were conducted at FPL running speed; $\dot{\phi}$ = 37,470 rpm = 3930 rad/sec. The data of Eq. (40) was used for all simulations. The proposed damper redesign of figure 7 includes a modification of the ball-bearing carrier to achieve the damper length of one inch given in Eq. (40). Maximization of the damper length is obviously desirable, since the damper forces are proportional to the length cubed.

The transient simulation model was first employed to verify the stability results of Chapter III. The results of the transient simulation model agreed in all respects with the linear stability analysis results of Chapter III. The simulation model was then employed to determine the effectiveness of the squeeze-film damper designs of figure 7 in stabilizing the rotor. The capabilities of the simulation model were required to account for the significant nonlinearities of the squeeze-film damper force definition in Eq. (37).

The imbalance used in the simulation model is as follows

$$\begin{array}{ll} \text{1st stage impeller,} & 2.86 \text{ gm in} \\ \text{2nd stage impeller,} & 2.96 \text{ gm in} \\ \text{3rd stage impeller,} & 3.52 \text{ gm in} \\ \text{2nd stage turbine,} & 2.74 \text{ gm in} \\ \text{1st stage turbine,} & 2.88 \text{ gm in} \end{array} \qquad (41)$$

The eccentricity distribution used to yield these imbalances was

$$\begin{array}{ll} \text{1st stage impeller,} & a_x = 3.57 \times 10^{-4} \text{in} \\ \text{2nd stage impeller,} & a_y = 3.68 \times 10^{-4} \text{in} \\ \text{3rd stage impeller,} & a_x = 4.02 \times 10^{-4} \text{in} \\ \text{2nd stage turbine,} & a_y = 3.05 \times 10^{-4} \text{in} \\ \text{1st stage turbine,} & a_x = -3.03 \times 10^{-4} \text{in} \end{array} \qquad (42)$$

The data of Eq. (41) was provided by Mr. B. Rowan, Rocketdyne, and includes tolerance stackup and reassembly imbalance. The imbalance distribution of Eq. (42) was selected to be representative, as opposed to a worst-case situation.

In addition to the imbalance distribution of Eq. (42), the HPFTP rotor is also subject to a hydrodynamic side load at the third-stage impeller discharge. The direction of this load is fixed with respect to the pump housing, and the load is defined here by

$$f_x = -6.721 \times 10^{-5} \dot{\phi}^2 \qquad (43)$$

where $\dot{\phi}$ is in rad/sec. This fixed direction side load is large in comparison to the imbalance loading of Eq. (42).

From a design viewpoint, the only variable which can be modified in the squeeze-film damper design is the clearance. The results of Eq. (39) in the preceding section indicate that the clearance of a squeeze-film damper should be minimized. The procedure followed in determining feasible minima for the pump- and turbine-end dampers consisted of running the simulation model with sufficient external damping to ensure stable synchronous motion, and then simply picking clearances that are sufficient to enclose the stable rotor orbits at the bearings.

Applying the above procedure to the situation of figure 4(a) ($k_{Sp} = k_{St} = 2.17 \times 10^5$ lb/in; $\zeta_1 = \zeta_2 = 0.0$) yields the following squeeze-film damper clearances

$$\begin{aligned} \delta_p(\text{pump}) &= .002 \text{ in} \\ \delta_t(\text{turbine}) &= .003 \text{ in} \end{aligned} \tag{44}$$

The frames of figure 8 indicate the results of a simulation run with these clearances for the squeeze-film dampers of figure 7. The initial conditions for this run are the final conditions of a run which was stabilized by adding external damping; however, the only damping acting on the rotor in figure 8 is that provided by the seals and the two squeeze-film dampers.

Figures 8(a) and (b) illustrate respectively the rotor-fixed modal coordinates q_{X1}, q_{X2}. Note that q_{X1} is approximately an order of magnitude larger than q_{X2}. The high-frequency oscillations in these modal coordinates are caused by the hydrodynamic side load of Eq. (43). If the rotor were excited solely by imbalance these variables

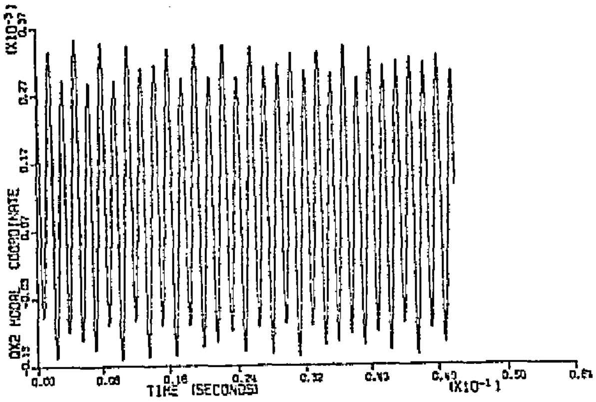

figure 8b

q_{X2} versus time for $k_s = 2.17 \times 10^5$ lb/in; $\zeta_1 = \zeta_2 = 0$.

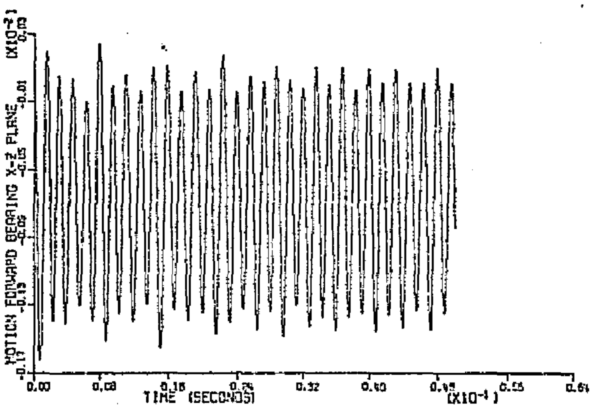

figure 8c

Rotor motion at the pump-end squeeze-film damper in the X-Z plane for $k_s = 2.17 \times 10^5$ lb/in; $\zeta_1 = \zeta_2 = 0$.

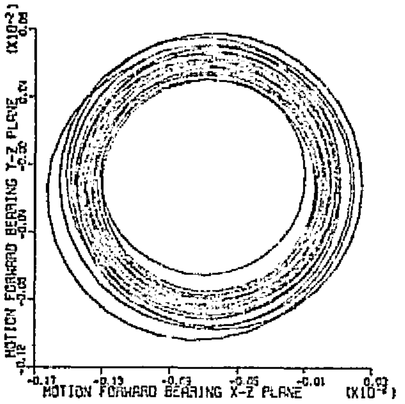

figure 8d

Rotor orbit at the pump-end squeeze-film damper for $k_s = 2.17 \times 10^5$ lb/in; $\zeta_1 = \zeta_2 = 0$.

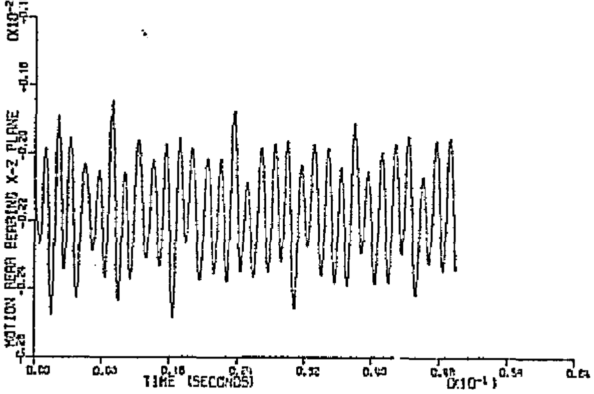

figure 8e

Rotor motion at the turbine-end squeeze-film damper in the X-Z plane for $k_s = 2.17 \times 10^5$ lb/in; $\zeta_1 = \zeta_2 = 0$.

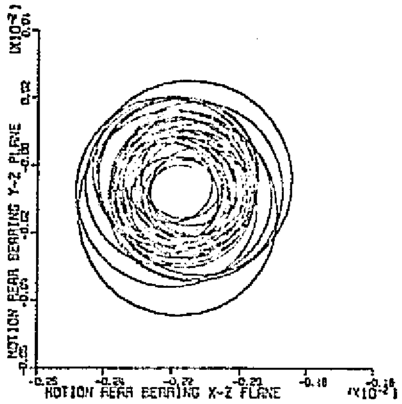

figure 8f

Rotor orbit at the turbine-end squeeze-film damper for $k_s = 2.17 \times 10^5$ lb/in; $\zeta_1 = \zeta_2 = 0$.

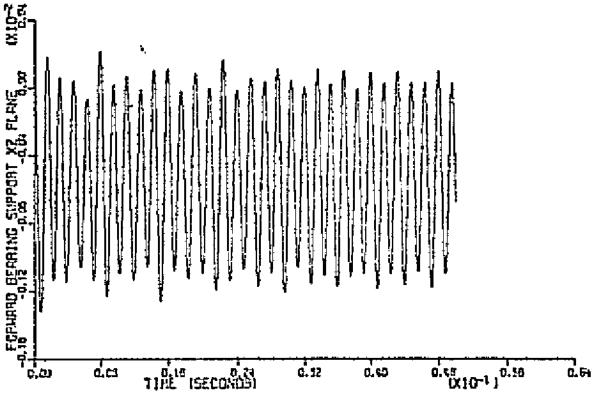

figure 8g

Pump-end squeeze-film damper cylinder motion in the X-Z plane for $k_s = 2.17 \times 10^5$ lb/in; $\zeta_1 = \zeta_2 = 0$.

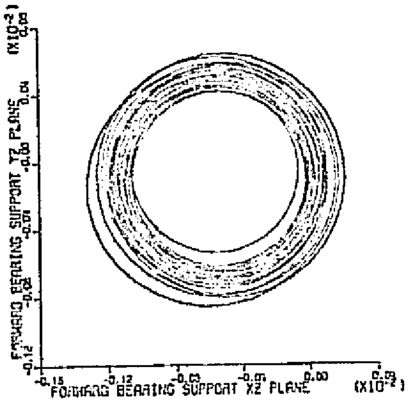

figure 8h

Pump-end squeeze-film damper sylinder orbit for $k_s = 2.17 \times 10^5$ lb/in; $\zeta_1 = \zeta_2 = 0$.

c

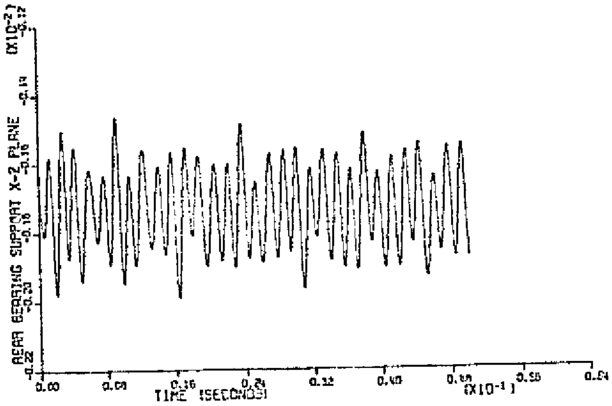

figure 8i

Turbine-end squeeze-film damper cylinder motion in the X-Z plane for $k_s = 2.17 \times 10^5$ lb/in; $\zeta_1 = \zeta_2 = 0$.

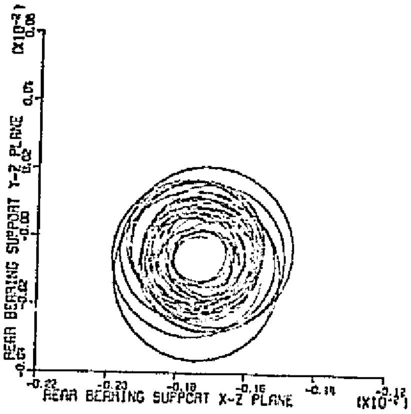

figure 8j

Turbine-end squeeze-film damper cylinder orbit for $k_s = 2.17 \times 10^5$ lb/in; $\zeta_1 = \zeta_2 = 0$.

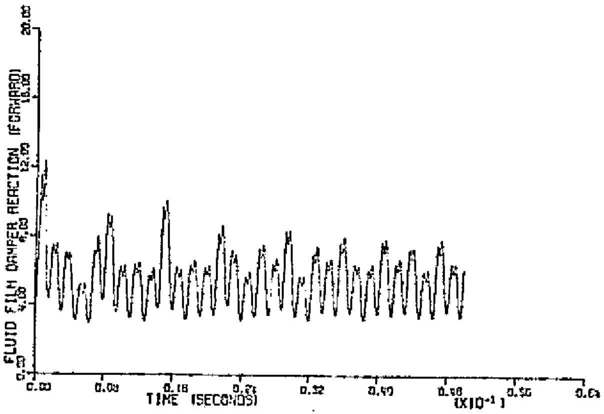

figure 8k

Pump-end squeeze-film damper reaction magnitude for $k_s = 2.17 \times 10^5$ lb/in; $\zeta_1 = \zeta_2 = 0$.

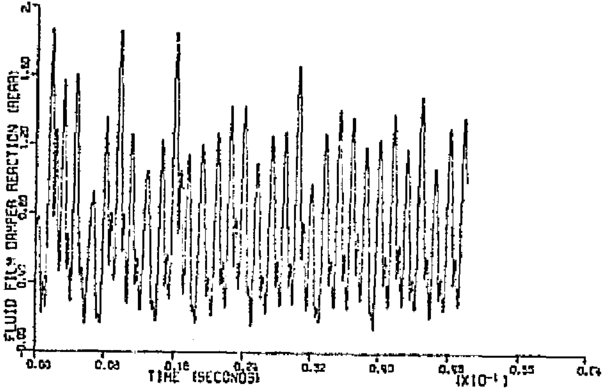

figure 81

Turbine-end squeeze-film damper reaction magnitude for $k_s = 2.17 \times 10^5$ lb/in; $\zeta_1 = \zeta_2 = 0$.

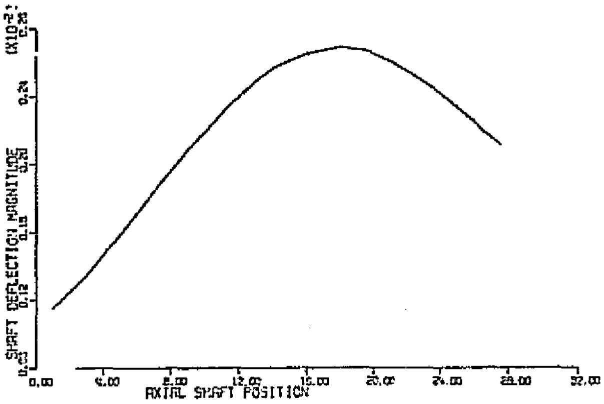

figure 8m

Rotor displacement magnitudes versus rotor axial position for $k_s = 2.17 \times 10^5$ lb/in; $\zeta_1 = \zeta_2 = 0$.

would be constant during synchronous precession of rotor. The results of figure 8(a) indicates that the squeeze-film dampers with the clearances of Eq. (42) have completely stabilized the first mode. However, figure 8(b) illustrates that the second mode has a subsynchronous oscillation which has limit cycled. Without the squeeze-film dampers, the first mode is unstable, while the second mode is stable.

Figures 8(c) and (d) illustrate the motion of the rotor at the pump bearing. Figure 8(c) demonstrates the motion of the rotor in the stationary X-Z plane, and 8(d) illustrates the rotor orbital motion. The static displacement of the rotor illustrated in these figures is caused by the hydrodynamic side load of Eq. (43). These figures illustrate that the pump end of the rotor is precessing synchronously.

Figures 8(e) and (f) are similar to figures 8(c) and (d), except that they illustrate rotor motion at the turbine-end bearing. Both of these figures indicate the presence of a subsynchronous whirl component that has limit cycled. They also indicate that the steady-state displacement of the rotor due to the hydrodynamic sideload is much larger at the turbine end of the rotor than at the turbine end. If only the bearing carrier structure stiffness is considered, this result would not be anticipated from the location of the side load, i.e., comparable magnitides would be expected for both ends. However, the result is explained by the additional stiffness provided by the seal coefficients of Table 5.

Figures 8 (g) and (h) illustrate the motion of the pump-end squeeze-film damper cylinder, while figures 8(i) and (j) illustrate the motion for the turbine-end squeeze-film damper. The results of these figures are basically similar to the rotor motion at these locations in figures 8(e) - (f). The large magnitude of the steady-state displacements in figures 8(i) and (j) precludes the use of a clearance smaller than δ_t = .003 in. Figures 8(g) - (j) demonstrate that the pump and turbine squeeze-film dampers are operating at eccentricities of 0.3 and 0.57, respectively.

Figures 8(k) and (l) illustrate the force magnitudes developed at the pump- and turbine-end squeeze-film dampers, respectively. The force magnitude at the pump-end squeeze-film damper is larger and more smoothly defined than for the turbine-end squeeze-film damper. This is the result of (a) a smaller clearance and eccentricity ratio for the pump-end squeeze-film damper, and (b) the synchronous motion of the pump-end of the rotor as opposed to the combined synchronous-subsynchronous motion of the turbine end.

Figure 8(m) illustrates the rotor displacement magnitudes as a function of axial position, which confirms the previous statement that the motion at the pump-end of the rotor is smaller than the turbine-end. It also demonstrates the influence of the hydrodynamic side load in causing large deflections at the approximate midspan of the rotor.

The maximum pump and bearing reactions accompanying the results of figure 8 were 240 and 440 lbs, respectively.

The required squeeze-film damper clearances for the "measured" bearing support stiffness results of figure 4(b) ($k_{Sp} = k_{St} = 1.4 \times 10^5$ lb/in; $\zeta_1 = \zeta_2 = .01$) are

$$\begin{aligned} \delta_p(\text{pump}) &= .002 \text{ in} \\ \delta_t(\text{turbine}) &= .0035 \text{ in} \end{aligned} \tag{45}$$

By comparison to Eq. (44), one observes that the turbine-end clearance has been increased from .003 in to .0035 in, while the pump-end clearance is unchanged. The frames of figure 9 indicate the results of a simulation run with these squeeze-film damper clearances.

Figures 9(a) and (b) illustrate, respectively, the modal coordinates q_{X1}, q_{X2}. The motion of these variables is similar to that of figures 8(a) and (b); however, q_{X1} now has a slight subsynchronous component, and the subsynchronous component of q_{X2} is more pronounced. The modal coordinate q_{X1} continues to be an order of magnitude greater than q_{X2}.

As in figure 8, the motion of the rotor and the squeeze-film damper cylinder at the same axial position are very similar, hence only the motion of the squeeze-film damper cylinders is illustrated in figure 9. The motion of the pump-end squeeze-film damper cylinder is illustrated in figure 9(c) and 9(d), and continues to be

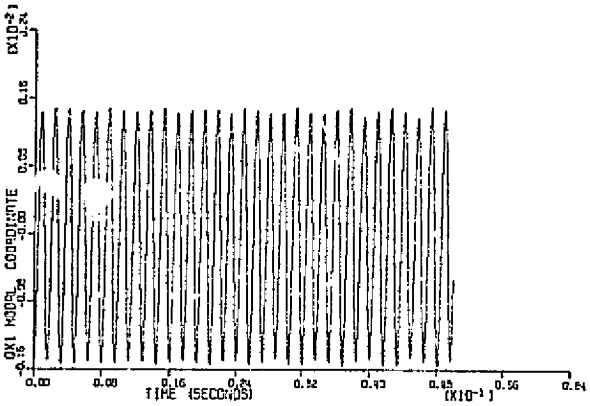

figure 9a

q_{X1} versus time for $k_X = 1.4 \times 10^5$ lb/in; $\zeta_1 = \zeta_2 = .01$.

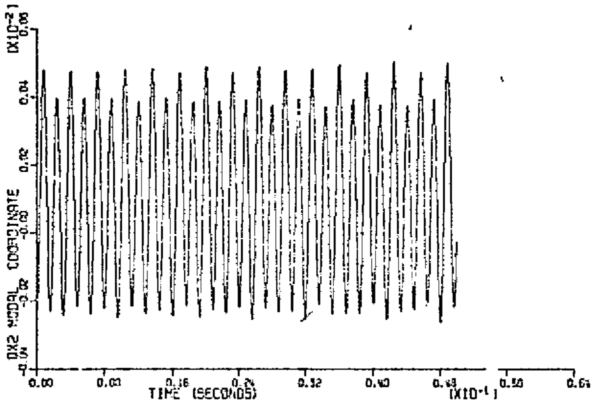

figure 9b

q_{X2} versus time for $k_X = 1.4 \times 10^5$ lb/in; $\zeta_1 = \zeta_2 = .01$.

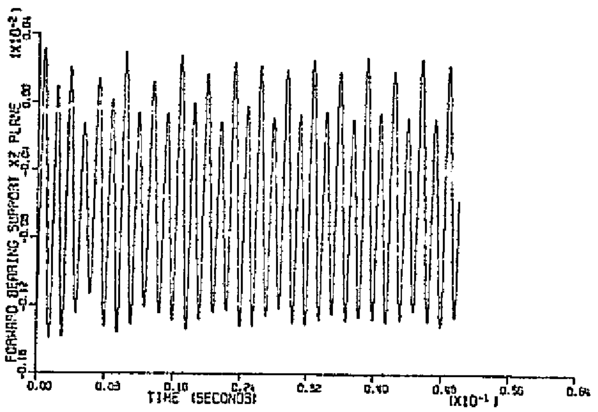

figure 9c

Pump-end squeeze-film damper cylinder motion in the X-Z plane for $k_s = 1.4 \times 10^5$ lb/in; $\zeta_1 = \zeta_2 = .01$.

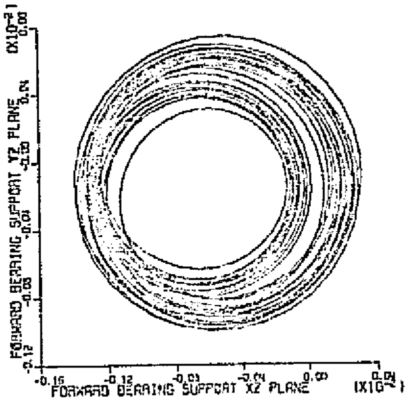

figure 9d

Pump-end squeeze-film damper cylinder orbit in the X-Z plane for $k_s = 1.4 \times 10^5$ lb/in; $\zeta_1 = \zeta_2 = .01$.

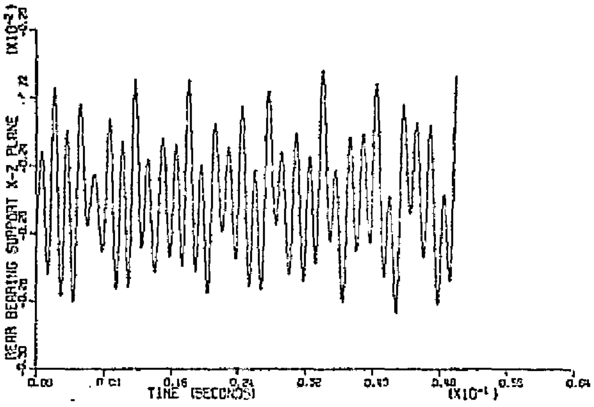

figure 9e

Turbine-end squeeze-film damper cylinder motion in the X-Z plane for $k_s = 1.4 \times 10^5$ lb/in; $\zeta_1 = \zeta_2 = .01$.

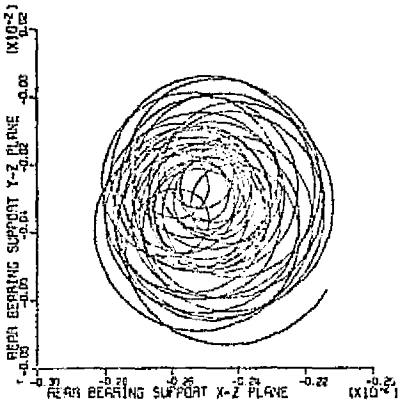

figure 9f

Turbine-end squeeze-film damper cylinder orbit for $k_s = 1.4 \times 10^5$ lb/in; $\zeta_1 = \zeta_2 = .01$.

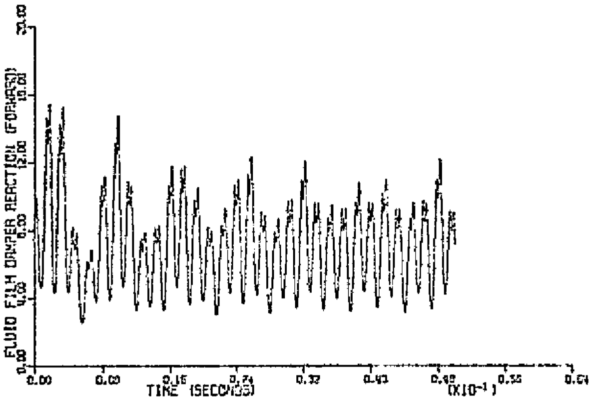

figure 9g

Pump-end squeeze-film damper reaction magnitude for $k_s = 1.4 \times 10^5$ lb/in; $\zeta_1 = \zeta_2 = .01$.

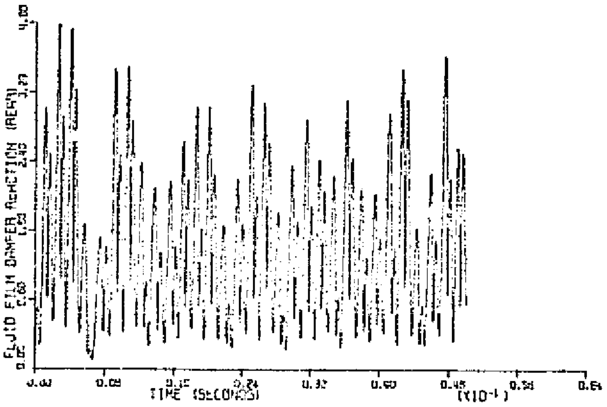

figure 9h

Turbine-end squeeze-film damper reaction magnitude for $k_s = 1.4 \times 10^5$ lb/in; $\zeta_1 = \zeta_2 = .01$.

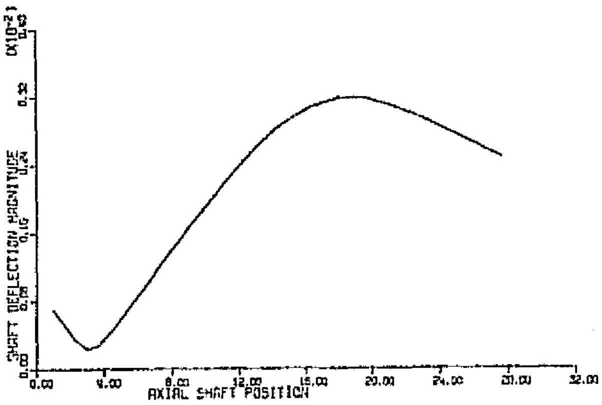

figure 9i

Rotor displacement magnitudes versus rotor axial position for $k_s = 1.4 \times 10^5$ bl/in; $\zeta_1 = \zeta_2 = .01$.

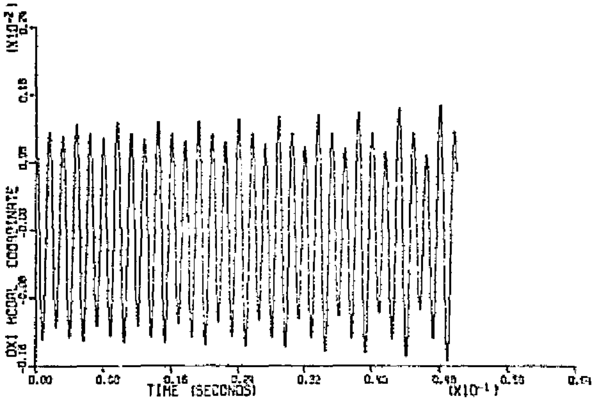

figure 10a

q_{X1} versus time for $k_{sp} = 1.4 \times 10^5$ lb/in; $k_{st} = 2.8 \times 10^5$ lb/in; $\zeta_1 = \zeta_2 = .01$.

basically synchronous, although a subsynchronous component is evident. The motion of the turbine-end squeeze-film damper is illustrated in figures 9(e) and (f). The subsynchronous component of this motion is now comparable to the synchronous component. The orbit amplitude of figure 9(f) is somewhat larger than the corresponding orbit of figure 8(j). The eccentricity ratios for the pump- and turbine-end squeeze-film dampers are 0.3 and 0.71, respectively.

The force amplitudes for the pump and turbine squeeze-film dampers are given as a function of time in figures 9(g) and (h), respectively, The amplitudes of both these forces are seen to have increased in comparison to figures 8(k) and (l). This result is explained by the fact that the rotor of figure 4(b) is less stable than the rotor of figure 4(c), and larger damping forces are required to contain it. The damper force at the turbine squeeze-film damper is in fact approximately twice as large in figure 9(h) as in figure 8(l), despite an increase in squeeze-film damper clearance from .003 in to .0035 in. However, this result is explained by the associated increase in eccentricity ratio from 0.57 to 0.71.

Figure 9(i) illustrates the rotor displacement amplitudes versus axial rotor position. When compared to figure 9(m), this figure explains why the clearance for the pump squeeze-film damper could remain at .002 in, despite a reduction in bearing support stiffness from 2.17 x 10^5

lb/in to 1.4×10^5 lb/in. Specifically, the amplitudes of the forward bearing continues to be small because the pump-end of the rotor has "crossed-over" the bearing centerline, and is now 180° out of phase with the turbine end of the rotor. The increase in rotor deflections caused by reducing the bearing support stiffness is primarily felt in the turbine end of the rotor.

One would not necessarily be convinced from the results of figure 9 that the unstable motion of the rotor has in fact been contained. However, the final values from the results of figure 9 were used as initial values for a second simulation run, and the results were basically unchanged.

An inspection of the results of figures 8 and 9 demonstrates that the turbine end of the rotor is more difficult to stabilize than the pump end, in part, because the amplitudes are larger and the turbine-end squeeze-film damper must accordingly have a larger clearance than the pump end. With this in mind, the bearing support stiffness pair

$$k_{Sp}(\text{pump}) = 1.4 \times 10^5 \text{ lb/in} \qquad (46)$$

$$k_{St}(\text{turbine}) = 2.8 \times 10^5 \text{ lb/in}$$

was investigated, since the increased turbine-bearing-support stiffness would presumably reduce the turbine-end amplitudes of the rotor, and allow a reduction in δ_t. This change in stiffness had a negligible direct influence on rotor stability. An unanticipated consequence of the change in stiffness of Eq. (46), was that the pump-end amplitudes were increased, and the pump-end squeeze-film damper clearance had to be increased. The resultant clearances were

δ_p(pump) = .0025 in
δ_t(turbine) = .003 in

Figure 10 illustrates the result of a simulation run with these clearances, the stiffnesses of Eq. (46), and $\zeta_1 = \zeta_2 = .01$. The initial conditions for this run were obtained from a previous run for which sufficient external damping was provided to stabilize the rotor.

Figures 10(a) and (b) illustrate the modal coordinates q_{X1}, q_{X2}. By comparison to the previous results for these variables in figures 8 and 9, both are seen to show a pronounced increase in their subsynchronous whirl component. This is particularly true for the variable q_{X2}. Note that q_{X1} continues to be an approximate order of magnitude larger than q_{X2}.

The motion for the pump-end and turbine-end squeeze-film damper cylinders are illustrated in figures 10(c), (d) and 10(e), (f); respectively. The motion is clearly unstable, with the subsynchronous component increasing exponentially. The damper forces for these squeeze-film dampers are illustrated in figures (g) and (h), and are also seen to be divergent.

One could argue that the results of figure 10 are not

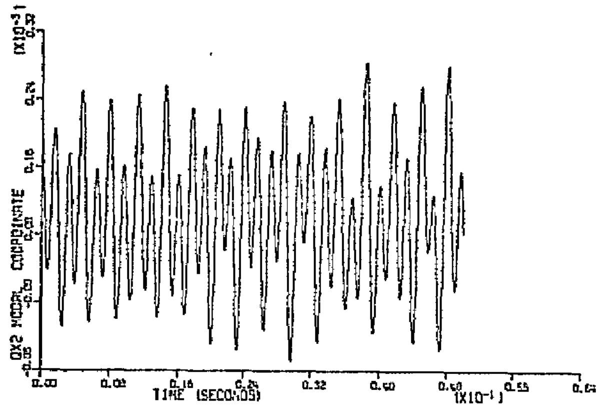

figure 10b

q_{X2} versus time for $k_{sp} = 1.4 \times 10^5$ lb/in; $k_{st} = 2.8 \times 10^5$ lb/in; $\zeta_1 = \zeta_2 = .01$.

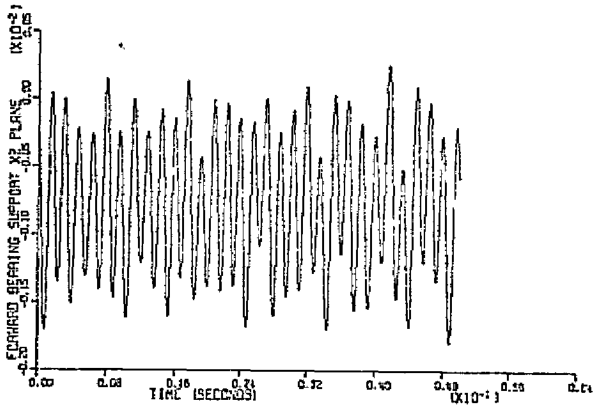

figure 10c

Pump-end squeeze-film damper cylinder motion in the X-Z plane for $k_{sp} = 1.4 \times 10^5$ lb/in; $k_{st} = 2.8 \times 10^5$ lb/in; $\zeta_1 = \zeta_2 = .01$.

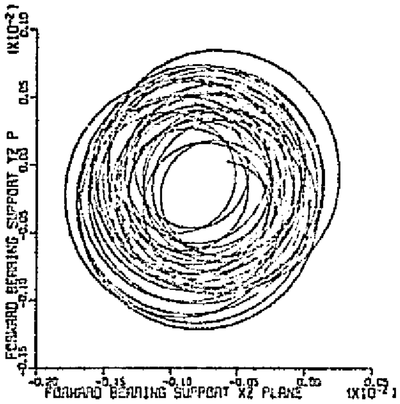

figure 10d

Pump-end squeeze-film damper orbit for $k_{sp} = 1.4 \times 10^5$ lb/in; $k_{st} = 2.8 \times 10^5$ lb/in; $\zeta_1 = \zeta_2 = .01$.

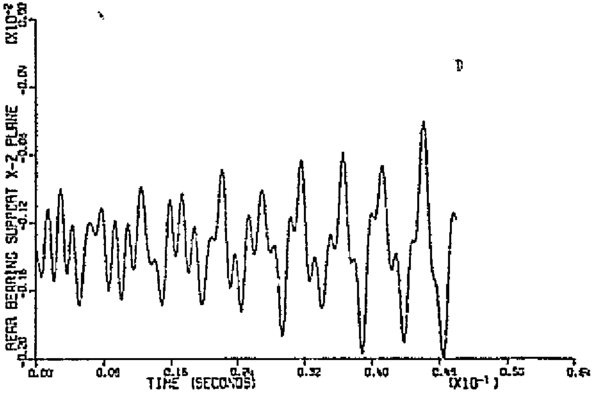

figure 10e

Turbine-end squeeze-film damper cylinder motion in the X-Z plane for $k_{sp} = 1.4 \times 10^5$ lb/in; $k_{st} = 2.8 \times 10^5$ lb/in; $\zeta_1 = \zeta_2 = .01$.

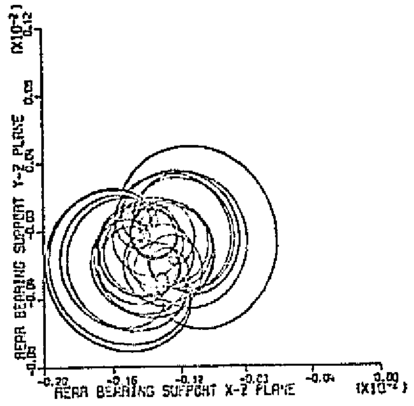

figure 10f

Turbine-end squeeze-film damper cylinder orbit for $k_{sp} = 1.4 \times 10^5$ lb/in; $k_{st} = 2.8 \times 10^5$ lb/in; $\zeta_1 = \zeta_2 = .01$.

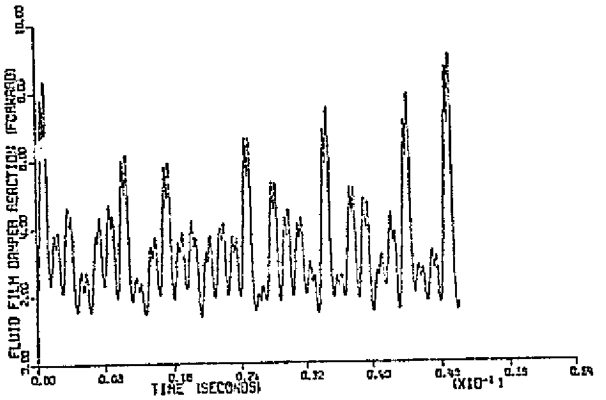

figure 10g

Pump-end squeeze-film damper reaction magnitude for $k_{sp} = 1.4 \times 10^5$ lb/in; $k_{st} = 2.8 \times 10^5$ lb/in; $\zeta_1 = \zeta_2 = .01$.

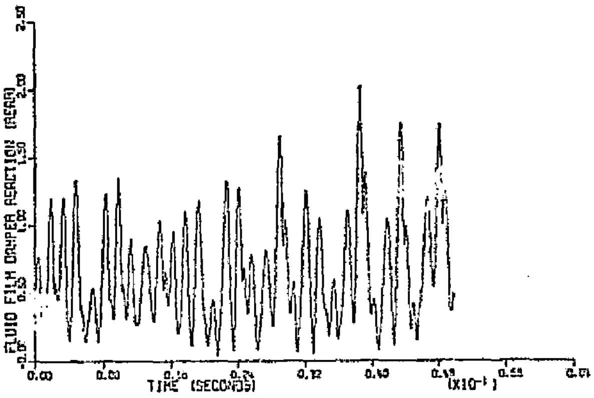

figure 10h

Turbine-end squeeze-film damper reaction magnitude for $k_{sp} = 1.4 \times 10^5$ lb/in; $k_{st} = 2.8 \times 10^5$ lb/in; $\zeta_1 = \zeta_2 = .01$.

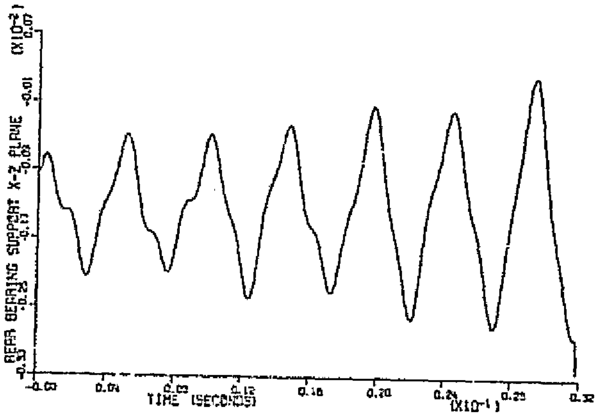

figure 11a

A continuation of figure 10c. Turbine-end squeeze-film damper cylinder motion in the X-Z plane for $k_{sp} = 1.4 \times 10^5$ lb/in; $k_{st} = 2.8 \times 10^5$ lb/in; $\zeta_1 = \zeta_2 = .01$.

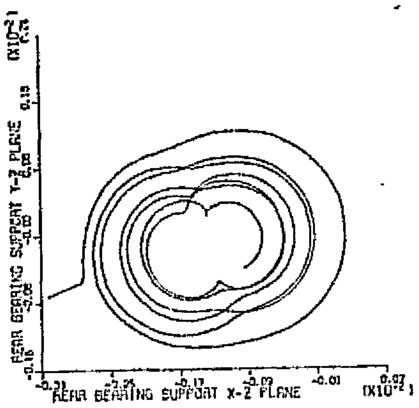

figure 11b

A continuation of figure 10f. Turbine-end squeeze-film damper cylinder orbit for $k_{sp} = 1.4 \times 10^5$ lb/in; $k_{st} = 2.8 \times 10^5$ lb/in; $\zeta_1 = \zeta_2 = .01$.

conclusive concerning rotor stability, since the rotor amplitudes could simply be approaching a large, but bounded-amplitude limit cycle. To obtain more conclusive results, final values from the run which produced the results of figure 10 were used as initial values for a second run. In this second run, the amplitudes continued to increase until the pump-end squeeze-film damper clearance was exceeded. Figures 11(a) and (b) illustrate the motion of the turbine-end squeeze-film damper cylinder from this simulation run. The unstable subsynchronous whirl in figure 11(a) is seen to be at 203 Hz. (12,200 rpm, or 1275 rad/sec). Hence, the unstable motion is clearly associated with the first mode, and the second mode is apparently stable.

The proposed squeeze-film damper redesign of figure 7 entails a reduction in flow area in annular flow passages of the pump, which has the undesirable side effect of constricting coolant flow. To circumvent this problem, a "partial" squeeze-film damper design was considered which incorporated small radial clearances over the half-circumference of the damper which had reduced steady-state clearances due to the hydrodynamic side load and large (.008 in) radial clearances over the portion which had increased radial clearances. This approach was followed for the turbine-end damper for each of the "fixed-clearance" situations of figures 8, 9, and 10. Specifically, simulation runs were performed with the large-clearance half circumference of the damper increased to .008 in, as compared to .003 in or .0035 in for the reduced-clearance half circumference of the damper. This "partial" squeeze-film damper design approach had no discernible effect on rotor stability. It does, however, have the practical advantages of increasing the supply of fluid for the damper, and allowing free coolant flow through the damper.

A review of the results of figures 8, 9, and 10 indicates that the squeeze-film damper designs of figure 7 can be of some value in controlling a rotor instability; however, the results are neither particularly encouraging nor conclusive. The efficacy of the damper is very dependent on the proper choice of clearance. Without some measured data to determine the amplitude of bearing carrier motion, it is going to be difficult to do more than guess at appropriate clearance values. Figures 10 and 11 illustrate the result of selecting damper clearances which are too large. Conversely, the selection of clearances which are too small would cause the dampers to "seize" or "lock-up", eliminating the soft-bearing design with its desirable critical-speed locations.

The simulation runs which yields the results of figures 8, 9, 10, and 11 were made on an IBM 360-165 computer. Each run involved 1010 integration steps with a constant integration stepsize of 5 x 10^{-5} seconds, and yielded 17 calcomp plots in addition to periodic printed output. The computer time requirements for each run was ap-

C.2

proximately 1 minute for execution and 16 seconds for compilation.

4.5 TRANSIENT SIMULATION OF HPFTP MOTION WITH SQUEEZE-FILM DAMPERS AND ASYMMETRIC SUPPORT STIFFNESS.

The results of Chapter III show that stiffness asymmetry in the bearing supports can improve rotor stability characteristics, and the preceeding section shows that squeeze-film damper forces can also improve rotor stability. The efficacy of a combination of these two approaches is considered in this section. The stiffness asymmetry set of Eq. (36) was considered for the following radial damper clearance choices:

(a) Pump-end damper.

reduced clearance half circumference = .002 in
enlarged clearance half circumference = .008 in

(b) Turbine-end damper.

reduced clearance half circumference = .003 in
enlarged clearance half circumference = .008 in

The simulation model was initially run with the internal damping factors $\zeta_1 = \zeta_2 = .01$ and sufficient external damping to ensure stability, and the final conditions of this run were then used as initial conditions for "stability" runs. The first such stability run was inconclusive, in that the rotor amplitudes increased, but it was not clear whether they would diverge or approach a stable limit. A subsequent run was made using the final values of the second run as initial conditions. The results of this run are contained in figure 12, and clearly indicate rotor instability. Figures 12(a) and (b) illustrate the modal coordinates q_{X1} and q_{X2}. A subsynchronous component is evident in both these figures. Motion in the X-Z plane for pump and turbine bearings are illustrated in figures 12(c) and (d). The turbine-bearing motion clearly shows the unstable nature of the motion with a whirl frequency at approximately 12,000 rpm. Hence, it is (again) the first mode that is unstable.

Although not illustrated, the simulation run which yielded the results of figure 12 were repeated with $\zeta_1 = \zeta_2 = 0.0$. For these damping coefficients, the motion is stable, although it contains a substantial subsynchronous component.

The results of this section indicate that the effectiveness of a redesign which combines the stiffness asymmetry of Eq. (36) and the squeeze-film damper design of figure 7 depends on the degree of rotor instability. Specifically, the addition of squeeze-film dampers can control the predicted instability of curve (a) in figure 4(a), but is not sufficient enough to control the predicted instability of curve (b).

4.6 HPOTP SIMULATION DEVELOPMENTS

The HPOTP transient simulation model of Ref. [1] was extended in this study to account for the seal coefficients of Tables 13-16. Also, the two-mode model of Ref. [1] was replaced here with a model for which four modes are re-

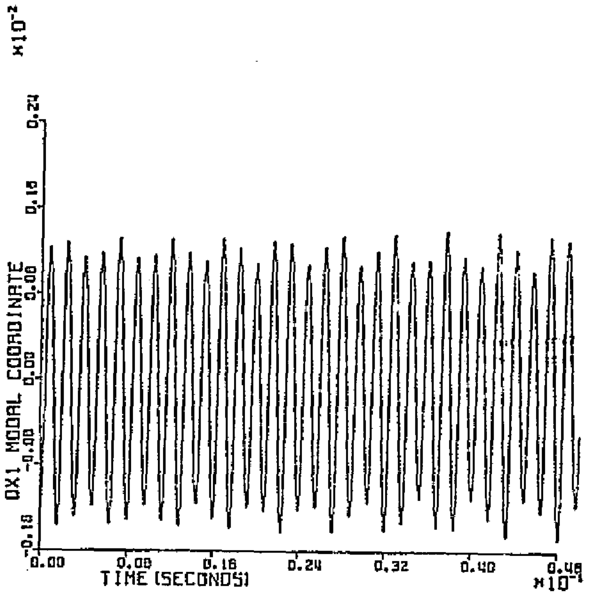

figure 12 a

q_{X1} versus time for the support stiffness definition of Eq. (36) with $\zeta_1 = \zeta_2 = .01$.

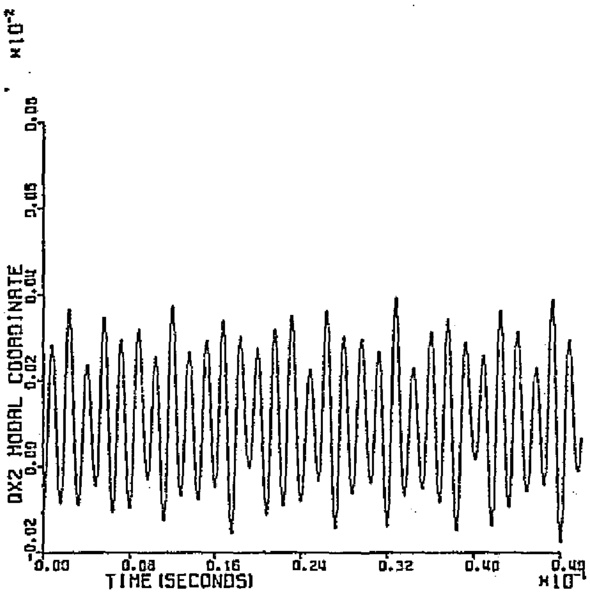

figure 12 b

q_{X2} versus time for the support stiffness definition of Eq. (36) with $\zeta_1 = \zeta_2 = .01$.

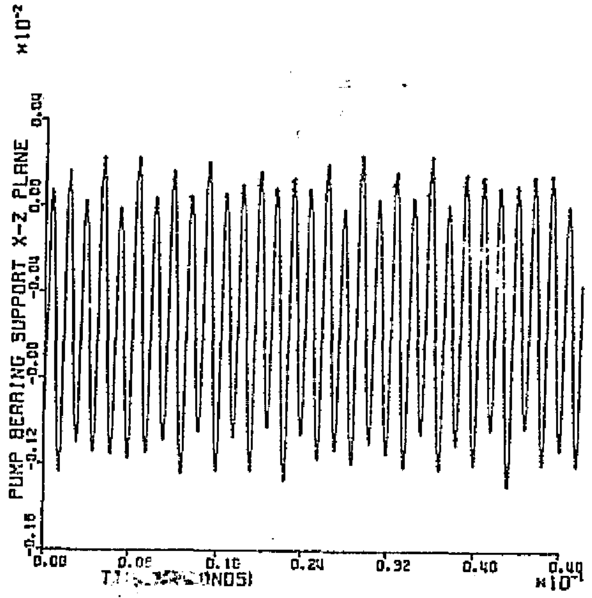

figure 12 c

Pump-end squeeze-film damper cylinder motion in the X-Z plane for the support stiffness definition of Eq. (36) with $\zeta_1 = \zeta_2 = .01$.

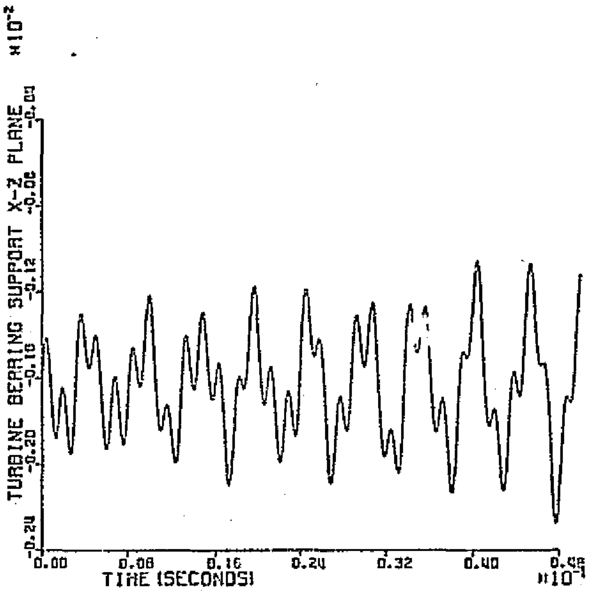

figure 12 d

Turbine-end squeeze-film damper cylinder motion in the X-Z plane for the support stiffness definition of Eq. (36), with $\zeta_1 = \zeta_2 = .01$.

tained for integration, and an additional 9 modes' static contribution are accounted for via a residual flexibility matrix. This improved model has been developed and verified; however, no specific use has been made of it in the present study. It is available for use in resolving rotordynamic problems which the SSME test program may uncover.

If the HPOTP should have a subsynchronous whirl problem as suggested by figures 5 the only design modifications which this investigator could presently propose for study would be modifications of the clearances between either (a) the outer races of the ball bearings and the bearing cartridge, or (b) the bearing cartridge and the pump housing. It is possible that the clearances at these locations could be used to develop stabilizing squeeze-film damper forces with liquid oxygen as the working fluid. Vance [18] discusses a squeeze-film damper design formed at the outer race of a ball bearing; however, his damper design is similar to that of figure 7 in that both an external oil supply and axial-flow seal constraints are required. No damper centering spring is attached to the ball-bearing outer-race in this design, however. Rocketdyne personnel have suggested that the present clearances will reduce the rotor amplitudes during critical speed transition below those predicted by this investigator [2-3]. Test results should be available shortly to settle this question and to determine whether a closer study of the potential value of these clearances is merited.

The model cited in the first paragraph of this section is not appropriate for the investigation of possible squeeze-film damp forces at the bearing outer-race clearances or bearing-cartridge clearances. Two additional HPOTP transient simulation models have accordingly been developed, based on free-free rotor modes, which can be used (if needed) to study possible squeeze-film forces associated with these clearances.

CHAPTER V

CONCLUSIONS AND RECOMMENDATIONS

Before summarizing the conclusions of this study, certain (possibly evasive) disclaimers are in order. The results of this study are at present generally without direct experimental verification. The study is almost entirely analytic in nature, and has entailed many assumptions and many points of judgement. An effort has been consistently made to specify the assumptions involved, and to provide sufficient data to allow interested parties to check the results, and to possibly reach conclusions different from those stated. The raw data used in this study have been supplied by Rocketdyne and NASA personnel based on best-available pre-test estimates. There has been a concious effort made throughout this study to avoid reaching dire conclusions based on a series of sequential "worst-case" assumptions. The study has been conducted to (hopefully) anticipate rotordynamic problems prior to testing, and to examine some alternative means for rectifying these problems should they occur. It has had the corollary objective of providing an improved understanding of the turbopump rotordynamic characteristics, which should increase the probability of a correct diagnosis of rotordynamic problems from test data.

The results of this study indicate a serious rotordynamic instability problem for the HPFTP. The predicted instability is caused by hydrodynamic seal forces and internal rotor damping.

A redesign of the bearing carrier structure to yield support stiffness asymmetry was considered, and substantially improves the stability characteristics of the HPFTP rotor by elevating the predicted onset speed of instability. However, an onset speed of instability continues to be predicted within the operating range for the degree of asymmetry which was used and assumed to be feasible in this study.

A redesign of the bearing carrier structures to yield squeeze-film damper surfaces (see figure 7) was investigated with mixed results. These dampers do generally improve rotor stability, but their sufficiency in this regard depends on the degree of rotor instability, and they can be overloaded.

A combination redesign incorporating support-stiffness asymmetry and squeeze-film dampers was also examined, again with mixed results. Specifically, a combination redesign is sufficient to control a degree of rotor instability, but can be overloaded.

In the event that a rotordynamic instability is encountered in the HPFTP test program, which is similar to that predicted in this study, the following recommendations are made:

(a) The bearing carriers should be redesigned to obtain stiffness asymmetry, and testing should then be conducted to determine the efficacy of this approach.

(b) Only if recommendation (a) is inadequate to control the instability should the proposed squeeze-film damper redesign of figure 7 be considered. A decision to implement the proposed redesign of figure 7 would necessarily need to be based on high quality test data, preferably proximity gauge data of actual rotor motion.

The results of this study concerning the HPOTP are not conclusive. A rotor instability associated with the first mode is possible, but is significantly less likely than for the HPFTP.

REFERENCES

1. D.W. Childs, "Two Jeffcott-Based Modal Simulation Models for Flexible Rotating Equipment," ASME Paper No. 74-WA/DE-17, 1974 Winter Annual Meeting, December 1974.

2. D.W. Childs, "Transient Rotordynamic Analysis for the Space Shuttle Main Engine High Pressure Turbopumps," Final Research Report 1973 NASA-ASEE Summer Faculty Fellowship Program, Auburn University Report No. 165-94, December 1973.

3. D.W. Childs, "Transient Rotordynamic Analysis for the Space Shuttle Main Engine High Pressure Oxygen Turbopump," AIAA Journal of Spacecraft and Rockets, Vol. 12, No. 1, Jan. 1975.

4. Black, H.F., "Calculation of Forced Whirling and Stability of Centrifugal Pump Rotor Systems," Paper No. 73-DET-31, ASME Vibration Conference, Cincinnati Ohio, September 1973.

5. Black, H.F., and Jensen, D.N., "Effects of High Pressure Ring Seals on Pump Rotor Vibrations," ASME Paper No. 71-WA/FE-38, 1971.

6. Black, H.F., and Jensen, D.N., "Dynamic Hybrid Properties of Annular Pressure Seals," Proc. I. Mech. E., Vol. 184, No. 3N, 1970.

7. Black, H.F., and Cochrane, E.A., "Leakage and Hybrid Bearing Properties of Serrated Seals in Centrifugal Pump," Paper G5, 6th International Conference on Fluid Sealing, Munich, German Federal Republic, Feb.27-March 2, 1973

8. Yamada, Y., "Resistance of Flow Through an Annulus with an Inner Cylinder Rotating," Bull. J.S.M.E., 1962, Vol. 5, No. 18, pp. 302-310.

9. McCarty, R.D., and Weber, L.A., "Thermophysical Properties of Parahydrogen from the Freezing Liquid Line to 5000 R for Pressures to 10,000 psia," National Bureau of Standards Technical Note 617, April 1972.

10. Roder, H.M., and Weber, L.A., "ASRDI Oxygen Technology Survey Volume I: Thermophysical Properties," NASA SP-3071, 1972.

11. Fasheh, J.J., "Review and Summary of Labyrinth Seal Theory and Design," TMR 2115-3351, Rocketdyne division of North American Rockwell, December 1972.

12. Gunter, Edgar J., Jr., "Rotor Bearing Stability", Proceedings of the First Turbomachinery Symposium, pp. 119-141.

13. Gunter, E.J., Jr., and Trumpler, P.R., "The Influence of Internal Friction on the Stability of High Speed Rotors with Anisotropic Supports," A.S.M.E. paper No. 69-Vibr-2.

14. Alford, J.S., "Protecting Turbomachinery from Self-Excited Rotor Whirl," A.S.M.E. Journal of Engineering for Power, pp. 333-344, October 1965.

15. Ehrich, F.F., a discussion of Ref. 13, A.S.M.E. Journal of Engineering for Power, pp. 333-344, October 1965.

16. Cunningham, R.E., Fleming, D.P., and Gunter, E.J. "Design of a Squeeze-Film Damper for a Multi-Mass Flexible Rotor," A.S.M.E. paper, Fourth Vibrations Conference, Whasington D.C., Sept 17-19, 1975.

17. Kirk, R. Gordon, and Gunter, E.J., Jr., "Transient Journal Bearing Analysis," NASA Contractor Report CR-1549, June, 1970.

18. Vance, John M., "High-Speed Rotor Dynamics--An Assessment of Current Technology for Small Turboshaft Engines," U.S. Army Air Mobility Research and Development Laboratory, USAAMRDL-TR-74-66, July 1974.

APPENDIX A: MODAL ROTORDYNAMIC FORMULATIONS

Childs in Ref. [1] developed the following two flexible rotor formulations based on the traditional Jeffcott-Green flexible rotor representation:

(a) a modal formulation based on the "conventional" Jeffcott flexible rotor model in which rotor deflections and rotations are defined in a stationary coordinate system, and

(b) a modal formulation for which the rotor deflections and rotations are initially defined in a rotor-fixed coordinate system.

In the present study, the "rotor-fixed" model was used for the transient simulation work, while the "conventional" model was used in stability analysis. A summary of the essential elements of these models follows.

A "CONVENTIONAL" MODAL JEFFCOTT MODEL

The rotor is modeled as a collection of n rigid bodies connected to each other by an elastic structure. The rotations and deflections of component rigid bodies are defined with respect to an inertial X, Y, Z coordinate system, where Z defines the rotor's nominal axis of rotation. The original structural-dynamic model for the rotor can be put into the form

$$\begin{bmatrix} [m] & 0 \\ 0 & [J] \end{bmatrix} \begin{Bmatrix} (\ddot{R}_X) \\ (\ddot{\beta}_Y) \end{Bmatrix} + [K_{XZ}] \begin{Bmatrix} (R_X) \\ (\beta_Y) \end{Bmatrix} = \begin{Bmatrix} (f_X) \\ (m_Y) \end{Bmatrix} + \ldots$$

$$\begin{bmatrix} [m] & 0 \\ 0 & [J] \end{bmatrix} \begin{Bmatrix} (\ddot{R}_Y) \\ (\ddot{\beta}_X) \end{Bmatrix} + [K_{YZ}] \begin{Bmatrix} (R_Y) \\ (\beta_X) \end{Bmatrix} = \begin{Bmatrix} (f_Y) \\ (m_X) \end{Bmatrix} + \ldots \qquad (A.1)$$

where (R_X), (β_Y) and (R_Y), (β_X) define the deflections and rotations in the X-Z and Y-Z planes, respectively. Further, [m] and [J] are the diagonal mass and diametral-moment-of-inertia matrices. The stiffness matrices $[K_{XZ}]$, $[K_{YZ}]$ define the nominal axisymmetric linear stiffness properties of the rotor-bearing structure. The vectors (f_X), (m_Y) and (f_Y), (m_X) are the external forces and moments in the X-Z and Y-Z planes, respectively.

Conventional eigenanalysis of the left hand side of equation (A.1) yields 2n eigenvalues λ_i^2 and 2n eigenvectors (A_i). The eigenvectors define the following coordinate transformations

$$(R_X) = [A_e](q_X), \quad (\beta_Y) = [A_\beta](q_X)$$

$$(R_Y) = [A_e](q_Y), \quad (\beta_X) = -[A_\beta](q_Y) \qquad (A.2)$$

From equation (A.2), the complete eigenvector matrices for the X-Z and Y-Z planes are defined by

$$[A_{XZ}] = \begin{bmatrix} A_e \\ A_\beta \end{bmatrix}, \quad [A_{YZ}] = \begin{bmatrix} A_e \\ -A_\beta \end{bmatrix}$$

The eigenvector matrices are normalized to satisfy

$$[A_e]^T[m][A_e] + [A_\beta]^T[J][A_\beta] = [U]$$

$$[A_{XZ}]^T[K_{XZ}][A_{XZ}] = [A_{YZ}]^T[K_{YZ}][A_{YZ}] = [\Lambda] \tag{A.3}$$

where [U] is the unity matrix, and $[\Lambda]$ is the diagonal matrix of eigenvalues λ_i^2.

The coordinate transformation defined by equations (A.2) and (A.3) yields the following modal vibration equations in the X-Z and Y-Z planes

$$(\ddot{q}_X) = (F_X) - \dot{\phi}[CM](\dot{q}_Y) - [\Lambda](q_X) + \dot{\phi}^2(P_X) + \ddot{\phi}(P_Y) - [C]\{(\dot{q}_X) + \dot{\phi}(q_Y)\}$$

$$(\ddot{q}_Y) = (F_Y) + \dot{\phi}[CM](\dot{q}_X) - [\Lambda](q_Y) + \dot{\phi}^2(P_Y) - \ddot{\phi}(P_X) - [C]\{(\dot{q}_X) - \dot{\phi}(q_X)\} \tag{A.4}$$

where ϕ defines the rotation of the rotor about the Z axis, and

$$[CM] = [A_\beta]^T[\bar{J}][A_\beta]$$

$$(P_X) = c\phi(P_X) - s\phi(P_y), \quad (P_Y) = s\phi(P_X) + c\phi(P_y)$$

$$(P_x) = [A_e]^T(ma_x) + [A_\beta]^T(J_{xz}) \tag{A.5}$$

$$(P_y) = [A_e]^T(ma_y) + [A_\beta]^T(J_{yz})$$

In the above, $[\bar{J}]$ is a diagonal matrix of polar moments of inertia $\bar{J}_i$, and the components of the vectors (ma_x), (ma_y), (J_{xz}), (J_{yz}) are $m_i a_x^i$, $m_i a_y^i$, $J^i{}_{xz}$, $J^i{}_{yz}$; respectively, where $a^i{}_x$, $a^i{}_y$ define the unbalance of component rigid body i, and $J^i{}_{xz}$, $J^i{}_{yz}$ are the products of inertia of rigid body i.

Returning to equations (A.4), the vectors (F_X), (F_Y)

are generalized modal forces defined by

$$
\begin{aligned}
(F_X) &= [A_e]^T(f_X) + [A_\beta]^T(M_Y) \\
(F_Y) &= [A_e]^T(f_Y) - [A_\beta]^T(M_X)
\end{aligned}
\tag{A.6}
$$

The matrix [C] in Eq. (A.4) defines the internal damping of the rotor, and has the diagonal elements $2\zeta_i \lambda_i$ where ζ_i is the damping factor. Component equations from (A.4) are

$$
\begin{aligned}
\ddot{q}_{Xi} &= F_{Xi} - \dot{\phi}\Sigma CM_{ij} q_{Yj} - \lambda_i{}^2 q_{Xi} - 2\zeta_i \lambda_i (\dot{q}_{Xi} + \dot{\phi} q_{Yi}) \\
&\quad + \dot{\phi}^2 P_{Xi} + \ddot{\phi} P_{Yi}; \qquad i = 1, 2, \ldots 2n \\
\ddot{q}_{Yi} &= F_{Yi} + \dot{\phi}\Sigma CM_{ij} \dot{q}_{Xj} - \lambda_i{}^2 q_{Yi} - 2\zeta_i \lambda_i (\dot{q}_{Yi} - \dot{\phi}\dot{q}_{Xi}) \\
&\quad + \dot{\phi}^2 P_{Yi} - \ddot{\phi} P_{Xi}; \qquad i = 1, 2, \ldots 2n
\end{aligned}
\tag{A.7}
$$

The governing equation for ϕ is

$$
\bar{J}\ddot{\phi} = M_z - (P_X)^T(\ddot{q}_Y) + (P_Y)^T(\ddot{q}_X) \tag{A.8}
$$

where $\bar{J}$ is the polar moment of inertia for the rotor, and M_z is the resultant spin-axis torque applied to the rotor.

A procedure for accommodating nonlinear or asymmetric bearings in this analysis can be explained by the following example. Suppose the bearing reaction at the ith station is defined by the components

$$
\begin{aligned}
Q_X{}^i &= G_X{}^i(R_X{}^i, R_Y{}^i, \dot{R}_X{}^i, \dot{R}_Y{}^i, \dot{\phi}) \\
Q_Y{}^i &= G_Y{}^i(R_X{}^i, R_Y{}^i, \dot{R}_Y{}^i, \dot{R}_Y{}^i, \dot{\phi})
\end{aligned}
\tag{A.9}
$$

A Taylor series expansion of these functions about $R^i{}_X = R^i{}_Y = 0$, $\dot{\phi} = \bar{\dot{\phi}}$ yields a reaction definition of the form

$$
\begin{Bmatrix} Q_X{}^i \\ Q_Y{}^i \end{Bmatrix} = K^i \begin{Bmatrix} R_X{}^i \\ R_Y{}^i \end{Bmatrix} + \begin{Bmatrix} g_X{}^i(R_X{}^i, R_Y{}^i, \dot{R}_X{}^i, \dot{R}_Y{}^i, \delta\dot{\phi}) \\ g_Y{}^i(R_X{}^i, (R_Y{}^i, \dot{R}_X{}^i, \dot{R}_Y{}^i, \delta\dot{\phi}) \end{Bmatrix} \tag{A.10}
$$

The matrix $[K^i]$ can be stated

$$[K^i] = [K^i{}_a] + [K^i{}_s]$$

$$= \begin{bmatrix} (k_{11} + k_{22})/2 & 0 \\ 0 & (k_{22} + k_{11})/2 \end{bmatrix} \tag{A.11}$$

$$+ \begin{bmatrix} (k_{11} - k_{22})/2 & 0 \\ 0 & (k_{22} - k_{11})/2 \end{bmatrix} .$$

The matrix $[K^i{}_a]$ is absorbed in the system stiffness matrices $[K_{XZ}]$, $[K_{YZ}]$ of equation (8), and the reaction terms of equation (20) become

$$\begin{Bmatrix} Q_X{}^i \\ Q_Y{}^i \end{Bmatrix} = [K_s{}^i] \begin{Bmatrix} R_X{}^i \\ R_Y{}^i \end{Bmatrix} + \begin{Bmatrix} g_X{}^i \\ g_Y{}^i \end{Bmatrix} \tag{A.12}$$

The negative of these terms are treated as external forces acting on body i, and are accounted for in the generalized force vectors of equation (A.8). Note that this development does not linearize the bearing characteristics. Specifically, the terms $g_X{}^i$, $g_Y{}^i$ account for the asymmetric, nonlinear, and speed dependent properties of the bearings. A similar procedure is followed to account for forces arising from seals and fluid-film dampers.

A "Rotor-Fixed" Modal Jeffcott Model

The equations of motion to be presented here differ from the preceeding in that they are stated in a rotor-fixed x, y, z coordinate system. The modal equations are

$$\begin{aligned} (\ddot{q}_x) &= (F_x) + \dot{\phi}\{2[U] - [CM]\}(\dot{q}_y) - \{[\Lambda] + \dot{\phi}^2[CK]\}(q_x) \\ &\quad - [C](\dot{q}_x) + \ddot{\phi}(P_y) + \dot{\phi}^2(P_x) \\ (\ddot{q}_y) &= (F_y) - \dot{\phi}\{2[U] - [CM]\}(\dot{q}_x) - \{[\Lambda] + \dot{\phi}^2[CK]\}(q_y) \\ &\quad - [C](\dot{q}_y) - \ddot{\phi}(P_x) + \dot{\phi}^2(P_y) \end{aligned} \tag{A.13}$$

where

$$\begin{aligned}(F_x) &= [A_e]^T(f_x) + [A_\beta]^T \\ (F_y) &= [A_e]^T(f_y) - [A_\beta]^T \\ [CK] &= [CM] - [U]\end{aligned} \qquad (A.14)$$

The component form of equation (A.13) is

$$\begin{aligned}\ddot{q}_{xi} &= F_{xi} + \dot{\phi}\Sigma(2\delta_{ij} - CM_{ij})\dot{q}_{yi} - \Sigma(\lambda_i{}^2\delta_{ij} + \dot{\phi}^2 CK_{ij})q_{xj} \\ &\quad 2\zeta_i\lambda_i\dot{q}_{xi} + \ddot{\phi}P_{yi} + \dot{\phi}^2 P_{xi}; \quad i = 1, 2, \ldots 2n \\ q_{yi} &= F_{yi} - \phi\Sigma(2\delta_{ij} - CM_{ij})q_{xj} - \Sigma(\lambda_i{}^2\delta_{ij} + \phi^2 CK_{ij})q_{yj} \\ &\quad 2\zeta_i\lambda_i\dot{q}_{yi} - \ddot{\phi}P_{xi} + \dot{\phi}^2 P_{yi}; \quad i = 1, 2, \ldots 2n\end{aligned} \qquad (A.15)$$

where δ_{ij} is the Kronecher delta.

The transformation from the rotor-fixed modal coordinates of Eq. (A.15) to the displacements and velocities of component rigid bodies is

$$\begin{aligned}(R_X) &= [A_e]\{c\phi(q_x) - s\phi(q_y)\} \\ (R_Y) &= [A_e]\{s\phi(q_x) + c\phi(q_y)\} \\ (\dot{R}_X) &= [A_e]\{c\phi(\dot{q}_x - \dot{\phi}q_y) - s\phi(\dot{q}_y + \dot{\phi}q_x)\} \\ (\dot{R}_Y) &= [A_e]\{s\phi(\dot{q}_x - \dot{\phi}q_y) + c\phi(\dot{q}_y + \dot{\phi}q_x)\}\end{aligned} \qquad (A.16)$$

and the differential equation for ϕ is

$$\begin{aligned}\bar{J}\ddot{\phi} &= M_z{}^r - 2\dot{\phi}\{(P_x)^T(\dot{q}_x) + (P_y)^T(\dot{q}_y)\} + (P_y)^T(\ddot{q}_x) \\ &\quad - (P_x)^T(\ddot{q}_y) - \dot{\phi}^2\{(P_y)^T(q_x) - (P_x)^T(q_y)\}\end{aligned} \qquad (A.17)$$

The procedure followed in past analyses has been to retain for integration those modes whose natural frequencies are less than the rotor's top running speed plus one or two modes above the top running speed. However in the present study, the residual flexibility method of Schwendler and Macneal was adapted to account for the "static" contribution of higher order modes. The technique employed is simple, and can be explained by considering the following structural-dynamic model

$$[M](\ddot{X}) + [K](X) = (f)$$

where [M] and [K] are n x n mass and stiffness matrices, and (X) and (f) are n x 1 vectors of generalized forces and displacements. Eigenalysis of this system yields a matrix of eigenvectors [A], and a diagonal matrix of eigenvalues $[\Lambda]$ which satisfy

$$[A]^T[M][A] = [U], \quad [A]^T[K][A] = [\Lambda]$$

Further, the coordinate transformation

$$(X) = [A](q) \tag{A.18}$$

yields the modal differential equations

$$(\ddot{q}) + [\Lambda](q) = [A]^T(f) \tag{A.19}$$

The first n modes are to be retained for integration, and the static contribution of the remaining (n-m) modes are defined by the algebraic equations

$$[\bar{\Lambda}](\bar{q}) = [\bar{A}]^T(f) \tag{A.20}$$

where the elements of $[\bar{\Lambda}]$ are the (m + 1) through n eigenvalues, and the matrix $[\bar{A}]^T$ contains the (m + 1) through n eigenvectors. Denoting the m modes to be retained for integration by $\tilde{q}$ yields the following complete model

$$(\ddot{\tilde{q}}) + [\tilde{\Lambda}](\tilde{q}) = [A]^T(f) \tag{A.21}$$

$$\begin{aligned}(x) &= [A]^T(\tilde{q}) + [\bar{A}](\bar{q}) \\ &= [A]^T(\tilde{q}) + [\bar{A}][\Lambda]^{-1}[\bar{A}]^T(f) \\ &= [A]^T(\tilde{q}) + [\Phi](f)\end{aligned}$$

The matrix $[\Phi]$ is called the residual flexibility matrix and accounts for the static contribution of higher order modes.

APPENDIX B SSME TURBOPUMP ROTOR/BEARING DYNAMIC MODELS

The structural dynamic models for the SSME turbopumps were developed by Rocketdyne personnel, and are discussed in detail in References [1], [2], with geometric, inertial, and eigen data provided. Hence, only a brief review of these models is given here, and only eifferent or additional data is provided.

HPFTP MODEL

The HPFTP rotor is modeled by twenty seven elastically connected rigid bodies while the bearing outer races and carrier structures are modeled by two point masses. In the model, the bearing support mass is attached to "ground" via a linear spring with coefficient k_S, and is attached to the rotor through a ball bearing of stiffness k_b as illustrated in figure B.1. The design value for k_S is

$$k_S = 2.17 \times 10^5 \text{ lb/in} \qquad (B.1)$$

The same bearing is used for both the pump- and turbine-end bearings, and the stiffness of this bearing is defined as a function of running speed $\dot{\phi}$ by

$$\begin{aligned} k_b &= a_0 + a_1\dot{\phi} + a_2\dot{\phi}^2 + a_3\dot{\phi}^3 \\ a_0 &= 1.475 \times 10^6 \text{ lb/in} \\ a_1 &= 162.8 \text{ lb/in} \qquad (B.2) \\ a_2 &= -.1559 \text{ lb sec}^2\text{/in} \\ a_3 &= 1.949 \times 10^5 \text{ lb/in} \end{aligned}$$

The basic eigendata used in this study was calculated for the support stiffness of Eq. (B.1), and a nominal bearing stiffness $\overline{k}_b = .891 \times 10^5$ lb/in, which is the approximate value of k_b in Eq. (B.2) at FPL. The first four eigenvectors are given in Table B.1, and correspond to the following natural frequencies.

$$\begin{aligned} \lambda_1 &= 921.5 \text{ rad/sec} = 8{,}800 \text{ rpm} \\ \lambda_2 &= 1589. \text{ rad/sec} = 15{,}200 \text{ rpm} \\ \lambda_3 &= 3558. \text{ rad/sec} = 34{,}000 \text{ rpm} \\ \lambda_4 &= 7486. \text{ rad/sec} = 71{,}500 \text{ rpm} \end{aligned} \qquad (B.3)$$

In addition, the next eight higher eigenvalues and their associated eigenvectors were used to calculate a residual flexibility matrix following the procedure outlined in Appendix A. The residual flexibility matrix was used in the simulation model, but was not used in stability studies. The residual correction technique was required to obtain the correct static load-deflection characteristics for the bearing support structure. Specifically, the first four modes of Table B.1 are not adequate to define the correct static load-deflection characteristics for the coordinates X_{b1}, X_{S1}, X_{b2}, X_{S2} of figure B.1. The first four modes give reasonably good results for the displacements along the rotor and at the bearings X_{b1}, X_{b2}; but are in error for both the bearing-support mass coordinates X_{S1}, X_{S2} and the relative motion between the shaft and the bearing-support masses. The explanation for this situation is that the eigenvectors which define the bearing support mass degree of freedom relative to the rotor are associated with natural frequencies that are much higher than the first four modes of Eq. (B.3). Correct static load-deflection properties were obtainable from the first eight modes. However (as noted above) the first twelve modes were employed in the transient model with the first four modes retained for integration and the next eight modes used to calculate the residual flexibility matrix [Φ].

HPOTP MODEL

The HPOTP rotor is modeled by thirteen elastically-connected rigid bodies. The HPOTP bearings are supported directly by the turbopump housing in contrast to the soft-bearing-mount design used for the HPFTP. The bearing stiffness definitions used for the pump and turbine bearings are

$$k_p(\text{pump}) = a_{p0} + a_{p1}\dot{\phi} + a_{p2}\dot{\phi}^2 + a_{p3}\dot{\phi}^3$$

$$\begin{aligned} a_{p0} &= 1.321 \times 10^6 \text{ lb/in} \\ a_{p1} &= 81.28 \text{ lb sec/in} \\ a_{p2} &= -.1857 \text{ lb sec}^2\text{/in} \\ a_{p3} &= 3.633 \times 10^{-5} \text{lb sec}^3\text{/in} \end{aligned} \qquad \text{(B.4)}$$

$$k_t(\text{turbine}) = a_{t0} + a_{t1}\dot{\phi} + a_{t2}\dot{\phi}^2 + a_{t3}\dot{\phi}^3$$

$$\begin{aligned} a_{t0} &= 1.799 \times 10^6 \text{ lb/in} \\ a_{t1} &= 105.2 \text{ lb sec/in} \\ a_{t2} &= -.3124 \text{ lb sec}^2\text{/in} \\ a_{t3} &= 5.912 \times 10^{-5} \text{ lb sec}^3\text{/in} \end{aligned} \qquad \text{(B.5)}$$

Eigenanalysis was performed for the nominal bearing stiffnesses $\bar{k}_p = \bar{k}_t = .891 \times 10^6$ lb/in. The first four eigenvalues for these nominal bearing stiffnesses are

$$
\begin{aligned}
\lambda_1 &= 1201.\ \text{rad/sec} = 11{,}466\ \text{rpm} \\
\lambda_2 &= 4082.\ \text{rad/sec} = 38{,}985\ \text{rpm} \\
\lambda_3 &= 5946.\ \text{rad/sec} = 56{,}780\ \text{rpm} \\
\lambda_4 &= 6440.\ \text{rad/sec} = 61{,}500\ \text{rpm}
\end{aligned}
\qquad \text{(B.6)}
$$

Their associated eigenvectors are given in Table B.2. Only the first four modes were used in the stability analysis of the HPOTP; however, the next nine modes were used to calculate a residual flexibility matrix for the transient simulation model.

ORIGINAL PAGE IS OF POOR QUALITY

	Zi	$[A_e]$				$[A_\beta]$ x 10			
1.	.9960	0.9118	-3.191	-5.264	-6.151	-1.077	-1.579	-7.339	-15.67
2.	2.296	1.0522	-2.986	-4.303	-4.081	-1.067	-1.573	-7.046	-13.89
3.	2.946	1.122	-2.884	-3.825	-3.083	-1.060	-1.576	-6.932	-13.11
4.	3.646	1.198	-2.774	-3.318	-2.063	-1.049	-1.578	-6.721	-11.85
5.	4.516	1.302	-2.662	-2.737	-0.9417	-0.9904	-1.657	-6.322	-9.230
6.	6.416	1.492	-2.353	-1.560	0.6904	-0.9153	-1.781	-6.057	-7.187
7.	7.966	1.636	-2.076	-0.6028	1.646	-0.8121	-1.923	-5.423	-3.919
8.	9.096	1.728	-1.856	0.0169	1.944	-0.7007	-2.064	-4.172	-1.005
9.	11.40	1.871	-1.355	0.9958	1.550	-0.5426	-2.247	-3.664	2.413
10.	12.95	1.949	-0.9946	1.513	0.8412	-0.4231	-2.333	-2.627	3.424
11.	14.16	1.985	-0.6963	1.719	0.1253	-0.1871	-2.487	-0.7536	4.388
12.	16.38	1.996	-0.1202	1.631	-1.135	-0.0177	-2.587	0.9279	4.064
13.	18.05	1.978	0.3211	1.341	-1.766	0.2111	-2.596	2.427	0.9768
14.	19.57	1.934	0.7201	0.8786	-1.810	0.5636	-2.569	3.360	-1.559
15.	21.00	1.871	1.094	0.2740	-1.415	0.5116	-2.472	4.036	-3.871
16.	22.25	1.807	1.414	-0.2870	-0.8413	0.4993	-2.532	4.346	-4.027
17.	23.50	1.738	1.727	-0.863	-0.1280	0.5178	-2.519	4.410	-5.229
18.	24.88	1.658	2.070	-1.508	0.7132	0.5317	-2.507	4.458	-5.512
19.	26.05	1.584	2.345	-2.022	1.388	0.5817	-2.436	4.446	-5.704
20.	26.62	1.539	2.467	-2.268	1.737	0.6048	-2.405	4.456	-5.856
21.	27.63	1.476	2.708	-2.726	2.370	0.61141	-2.399	4.474	-5.969
22.	4.246	1.260	-2.690	-3.020	-1.666	-1.067	-1.512	-6.497	-1.174
23.	7.496	1.591	-2.163	-0.9348	1.350	-0.9234	-1.806	-6.211	-5.932
24.	10.40	1.822	-1.588	0.6782	2.053	-0.6562	-2.150	-4.560	1.007
25.	12.88	1.949	-1.017	1.528	1.046	-0.3601	-2.439	-2.184	6.396
26.	15.35	1.994	-0.4035	1.784	-0.7409	-0.0819	-2.601	0.2458	6.487
27.	17.75	2.005	0.2402	1.386	-1.830	0.1976	-2.642	2.429	2.023
28.	3.646	0.9611	-2.236	-2.751	-1.952				
29.	26.62	1.234	1.986	-1.867	1.581				

TABLE B.1 HPFTP Rotating Assembly Eigenvectors.

	Zi	[A_e]				[A_β]			
1.	1.875	.0530	-1.030	7.372	3.910	.0798	-.7844	1.569	1.338
2.	2.920	-.0304	-.2070	5.669	2.475	.0798	-.7818	1.549	1.322
3.	3.930	-.1110	.5861	3.986	1.075	.0797	-.7684	1.392	1.218
4.	4.800	-.1847	1.275	2.879	.0386	.0779	-.7368	1.133	1.032
5.	6.430	-.3187	2.469	1.875	-1.158	.0337	-.3690	.4645	.1647
6.	9.600	-.3337	3.352	.9114	-1.059	-.0074	-.1227	.3981	-.1951
7.	13.20	-.2052	2.982	-.4729	.3777	-.1974	.2498	.2140	-.4429
8.	14.75	.1795	2.301	-.7391	1.178	-.2597	.2899	.1428	-.4321
9.	15.87	.5329	1.974	-.8999	1.720	-.3400	.2622	.1073	-.3729
10.	16.93	.9266	1.741	-1.027	2.177	-.3794	.2399	.0578	-.2605
11.	18.37	1.527	1.448	-1.093	2.547	-.4244	.2337	-.0426	-.0040
12.	20.10	2.349	1.060	-.9141	2.313	-.4704	.2648	-.2367	.5294
13.	22.25	3.404	.4901	-.2110	.0529	-.4932	.3131	-.4137	1.034

TABLE B.2 First Four Eigenvectors HPOTP.